Tectonics®

RESEARCH ARTICLE
10.1029/2022TC007491

Key Points:

- We perform single and two-stage analog and numerical models of Rift-Rift-Rift triple junctions
- Models show that differential velocity of extension between the plates is key for the geometry of fault patterns at triple junctions
- Two-stage models shed light on the geometry and evolution of the Afar triple junction

Correspondence to:

D. Maestrelli,
daniele.maestrelli@gmail.com;
daniele.maestrelli@igg.cnr.it

Citation:

Maestrelli, D., Brune, S., Corti, G., Keir, D., Muluneh, A. A., & Sani, F. (2022). Analog and numerical modeling of Rift-Rift-Rift triple junctions. *Tectonics*, *41*, e2022TC007491. https://doi.org/10.1029/2022TC007491

Received 3 JUL 2022
Accepted 21 SEP 2022

Author Contributions:

Conceptualization: D. Maestrelli, S. Brune, G. Corti, D. Keir, A. A. Muluneh, F. Sani
Data curation: D. Maestrelli
Formal analysis: D. Maestrelli, S. Brune, G. Corti, D. Keir, A. A. Muluneh, F. Sani
Funding acquisition: G. Corti, D. Keir
Investigation: D. Maestrelli, S. Brune, G. Corti, D. Keir, A. A. Muluneh, F. Sani
Methodology: D. Maestrelli, S. Brune, G. Corti, A. A. Muluneh, F. Sani
Project Administration: G. Corti, D. Keir
Resources: G. Corti, D. Keir
Supervision: G. Corti
Validation: D. Maestrelli, S. Brune, G. Corti, D. Keir, A. A. Muluneh, F. Sani
Visualization: D. Maestrelli, S. Brune
Writing – original draft: D. Maestrelli, S. Brune, G. Corti, D. Keir, A. A. Muluneh, F. Sani

Analog and Numerical Modeling of Rift-Rift-Rift Triple Junctions

D. Maestrelli[1], S. Brune[2,3], G. Corti[1], D. Keir[4,5], A. A. Muluneh[2,6], and F. Sani[1,4]

[1]CNR-IGG, Consiglio Nazionale delle Ricerche, Istituto di Geoscienze e Georisorse, Firenze, Italy, [2]Helmholtz-Centre Potsdam, GFZ German Research Centre for Geosciences, Potsdam, Germany, [3]Institute of Geosciences, University of Potsdam, Potsdam, Germany, [4]Dipartimento di Scienze della Terra, Università di Firenze, Firenze, Italy, [5]School of Ocean and Earth Science, University of Southampton, Southampton, UK, [6]School of Earth Sciences, Addis Ababa University, Addis Ababa, Ethiopia

Abstract Rift-Rift-Rift triple junctions are key features of emergent plate boundary networks during fragmentation of a continent. A key example of such a setting is the Afar triple junction where the African, Arabian and Somalian plates interact. We performed analog and numerical models simulating continental break-up in a Rift-Rift-Rift setting to investigate the resulting structural pattern and evolution. We modified the ratio between plate velocities, and we performed single-stage (with all plates moving at the same time) and two-stage (where one plate first moves alone and then all the plates move simultaneously) models. Additionally, the direction of extension was changed to induce orthogonal extension in one of the three rift branches. Our models suggest that differential extension velocities in the rift branches determine the localization of the structural triple junction, which is located closer to the rift branch experiencing slower extension velocities. Furthermore, imposed velocities affect the deformation resulting in end-member fault patterns. The effect of applying similar velocities in all rift arms is to induce a symmetric fault pattern (generating a Y-shaped geometry). In contrast, a faster plate generates structures trending orthogonal to dominant velocity vectors, while faults associated with the movement of the slower plates remain subordinate (generating a T-shaped pattern). Two-stage models reveal high-angle faults interacting at the triple junction, confirming that differential extension velocities strongly affect fault patterns. These latter models show large-scale similarities with fault patterns observed in the Afar triple junction, providing insights into the factors controlling the structural evolution of this area.

Plain Language Summary When continents break-up a rift valley can form and eventually grow to form an ocean. For particular conditions, more than two tectonic plates can be involved in this process. In this case, a "triple junction" is formed that consists of three rift branches. This process shaped the Afar region, where the movement of the Arabian, African, and Somalian plates, which separate at different rates of motion, created the Gulf of Aden, Red Sea, and Ethiopian rifts. The way in which triple junctions work can be difficult to study due to their large extent and several million year-long activity. Therefore, we performed physical laboratory experiments and numerical experiments on the computer to investigate how triple junction form. We performed models with different rates of motion for the three plates, simulating one or two tectonic stages. The models show that the difference in the rate of motion between the three plates is the main control on the distribution and type of faults forming at triple junctions. Our results suggest that the fault pattern at the Afar triple junction observed nowadays may be explained by two tectonic stages and a lower extension rate occurring between the African and Somalian plates.

1. Introduction

Triple junctions involve the movement of three tectonic plates, and therefore represent one of the most challenging settings to understand deformation processes (e.g., Kleinrock & Morgan, 1988; McKenzie & Morgan, 1969; Patriat & Courtillot, 1984). McKenzie and Morgan (1969) identified 16 possible cases of triple junctions, among which the only stable case for all velocity conditions is the extensional Ridge-Ridge-Ridge triple junction (RRR), in which the three plates move away from each other. For this reason, RRR junctions can be preserved independent of the individual extension directions, and therefore they may exhibit symmetrical settings (with rift branches at 120°) as well as extremely asymmetric geometries.

Writing – review & editing: D. Maestrelli, S. Brune, G. Corti, D. Keir, A. A. Muluneh, F. Sani

Extensional triple junctions most commonly develop in oceanic lithosphere and are therefore normally located below sea level (McKenzie & Morgan, 1969). They are consequently difficult to observe and analyze in detail. The Afar depression in Ethiopia is the most prominent emerged example of an extensional triple junction and forms from the movement among the Nubian, Somalian, and Arabian plates (e.g., Burke & Dewey, 1973; Hayward & Ebinger, 1996; Manighetti et al., 1997; Tesfaye et al., 2003; Wolfenden et al., 2004). In Afar, extension has not reached the oceanic stage yet (despite the Gulf of Aden already being in a mature stage of oceanic spreading Leroy et al., 2012), and therefore affects the continental lithosphere defining a Rift-Rift-Rift (rather than Ridge-Ridge-Ridge) triple junction. Despite their kinematic similarity, Rift-Rift-Rift and Ridge-Ridge-Ridge triple junctions are governed by different physics (plate fragmentation vs. plate accretion processes; Gerya & Burov, 2018) and therefore exhibit distinct structural differences.

Analog models have been widely applied to the analysis of tectonic processes; however, triple junctions are difficult to investigate in the laboratory, due to the complexity associated with the movement of three plates. For this reason, few studies have attempted such modeling (e.g., Khalil et al., 2021; Oliveira et al., 2021; Souriot & Brun, 1992) and only reproduced the movement of one or two plates out of the three. Instead, triple junction dynamics have so far been investigated with kinematic reconstructions (e.g., Jestin & Huchon, 1992) and numerical models (Dordevic & Georgen, 2016; Gerya & Burov, 2018; Karaoğlu et al., 2016; Koptev et al., 2018). However, the numerical models have focused on thermal interactions between plumes and lithosphere and implications for broad scale strain localization, and did not address fault development, interaction and evolution (e.g., Burke & Dewey, 1973; Gerya & Burov, 2018; Koptev et al., 2018).

In this paper we focus on Rift-Rift-Rift triple junctions, presenting 12 analog models and four numerical models aimed at simulating the structural evolution and fault interactions in these complex settings. In our setup, we overcame the technical problem of three simultaneously divergent plates, and we investigate how parameters such as the geometry (symmetry/asymmetry) of the system, the difference in velocity of motion of the plates or the evolution of extension (single-stage vs. multi-stage extension) may affect the resulting structural pattern. We show, in a theoretical perspective, how geometric end-members can be defined on the basis of fault interaction at the triple junction, and how the system evolves as one of the above-mentioned parameters is changed. Our analog and numerical models provide theoretical insights into RRR triple junction dynamics, and we then use the appropriate model scenarios for the Afar Rift-Rift-Rift triple junction in order to provide key insights into the major factors responsible for the observed structural configuration (e.g., Almalki & Betts, 2021; Koptev et al., 2018; Souriot & Brun, 1992; Tesfaye et al., 2003).

2. Methodology and Modeling Strategy

First we describe the methodology adopted for the analog and numerical modeling. All the data produced, supporting the results and discussion, are free to download from the data set described in Maestrelli et al. (2022).

2.1. Analog Modeling

The analog modeling experiments were carried out at the TOOLab (Tectonic Modeling Laboratory), which is a joint laboratory between the Department of Earth Sciences of the "Università di Firenze" and the "Istituto di Geoscienze e Georisorse" of the "Consiglio Nazionale delle Ricerche," Italy. Model setup consisted of three moving plates connected with an elastic band. Their movement was electronically controlled by stepper-motors. The models were built on top of this deformation apparatus and the deformation was monitored via automatic top-view photos and perspective photo acquisition, for 2D and 3D quantification of the deformation. A detailed description of the deformation apparatus and the analog modeling technique is provided in the following paragraphs.

2.1.1. Analog Modeling Setup and Materials

We designed a modeling setup involving three moving plates able to simulate the mechanics of a Rift-Rift-Rift triple junction (Figure 1). In our setup, a reference moving plate (MP1) is pulled by a stepper motor at the constant velocity of 10 mm/hr while the other two moving plates (MP2 and MP3) are controlled by a second stepper motor (Figure 1). MP2 and MP3 velocity (the same for both) and direction of movement were changed depending on the models and the experimental Series (see Section 2.3).

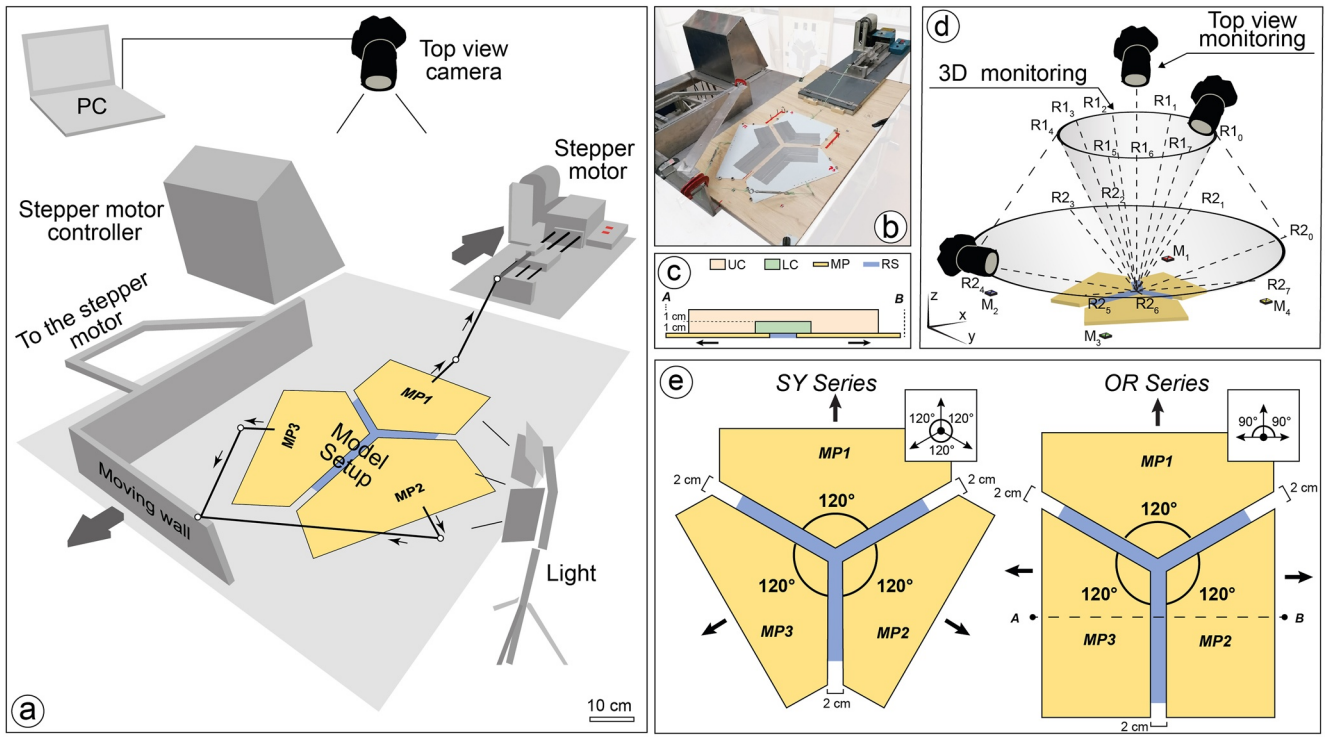

Figure 1. Analog modeling and monitoring setup. (a) Sketch of the deformation apparatus shown in (b). Plate movement was obtained via two stepper motors. A first one controls the velocity of the reference moving plate MP1. A second motor pulls a moving wall to which the other two moving plates (MP2 and MP3) are hinged via cables. The movement direction can be adjusted by guiding the plates through pivots and by changing the direction of extension through cable orientation. (c) Schematic cross section of model setup. UC, Upper Crust; LC, Lower Crust; MP, Moving Plate; RS, Rubber Sheet. Cross section trace location is shown in (e). (d) Sketch of the monitoring apparatus used for top view and perspective photo acquisition. These latter were used for photogrammetric reconstruction of model DEMs. See Maestrelli et al. (2021a, 2021b) for a detailed description of photogrammetric parameters and methodology. (e) Sketch of the two experimental series performed in this work; SY, symmetric experimental Series; OR, orthogonal Series. Blue area marks the rubber sheet position.

The moving plates were connected with a 0.1 mm-thick elastic latex band, here referred to as rubber sheet (RS, shown in purple in Figure 1), placed in a 2 cm-wide gap between the three Plexiglas moving plates (Figure 1b). This elastic band is used to distribute deformation at the triple junction and inside the rift branches. On top of this setup, a 1 cm-thick ductile layer of PDMS-Corundum sand mixture was leveled to simulate the behavior of the Lower Crust (LC). This mixture is composed of a ≈1:1 proportion in weight of Polydimethylsiloxane silicone (PDMS) and Corundum sand, characterized in Maestrelli et al. (2020) and already used in Wang et al. (2021). Parameters for this modeling material are reported in Table 1. This layer is placed on the area covering the RS, extending ca. 1 cm on each side. This was done to keep the deformation localized on the area of interest (similarly to this, in numerical models a randomized pattern of week seeds was used to properly initiate deformation in the triple junction area; see Section 2.2). Above this level, a 1 cm-thick brittle layer of sand mixture was poured and leveled to reproduce the brittle behavior of the Upper Crust (UC). In particular, we used the Qz-KFeld 70:30 (% in weight) sand mixture characterized in Montanari et al. (2017) and Del Ventisette et al. (2019). This sand mixture is composed of 70% well-rounded Quartz Fontainebleau sand grains (provided by Sibelco Italia S.p.A.) and the remaining 30% is K-feldspar superfine angular sand (produced by AKW Kaolin, Germany). Material parameters are summarized in Table 1. Models were deformed with incremental steps of deformation of 0.7 cm, taking as reference the movement of MP1. After each deformation step a <1 mm-thick layer of sand mixture was sieved and leveled to highlight fault reactivation during subsequent steps, to simulate natural sedimentation and to correctly scale fault displacement.

2.1.2. Scaling

Analog models need to achieve the correct similarity in terms of length, rheology, kinematic and dynamic evolution in order to reproduce a realistic replica of natural conditions (Hubbert, 1937; Ramberg, 1981; Weijermars & Schmeling, 1986). To perform the scaling calculations, we have taken Model A-SY-2 as the reference.

Table 1
Parameters of Experimental Materials and Scaling Ratios for the Analog Models

Analog material and parameter		Model	Nature	Model/Nature ratio
Qz-K-feldspar sand mixture (70:30% in weight) (simulates the Upper Crust - UC)	Density ρ_{UC} (kg m^{-3})	1,408	~2,700	$\rho^* \sim 0.52$
	Internal friction coefficient μ	0.83[a]	0.85	$\mu^* \sim 1$
	Cohesion c (Pa)	~9.5	$\sim 1 \times 10^7$	$c^* \sim 9.5 \times 10^{-7}$
	Thickness h_{UC} (m)	0.01	20,000	$h^* = 5 \times 10^{-7}$
PDMS-Corundum (~1:1% in weight) (simulates the Lower Crust - LC)	Density ρ_{LC} (kg m^{-3})	1,440	~2,760	$\rho^* \sim 0.52$
	Viscosity η_{LC} (Pa s)	1.6×10^5	10^{22}–10^{23}	$\eta^* = 1.6 \times 10^{-17}$–$1.6 \times 10^{-18}$
	Thickness h_{LC} (m)	0.01	20,000	$h^* = 5 \times 10^{-7}$
Length l (m)	0.01	20,000	$l^* = 5 \times 10^{-7}$	
Gravity g (m s^{-2})	9.81	9.81	$g^* = 1$	
Stress σ (Pa)			$\sigma^* \sim 2.6 \times 10^{-7}$	
Velocity, v (m s^{-1})	2.8×10^{-6}	3.4×10^{-11}–3.4×10^{-10} (≈1.1–11 mm yr^{-1})	$v^* = \sigma^* l^* / \eta^* = 8{,}125 - 8{,}1250$	

Note. The asterisk (*) denotes the ratio between model and nature for a given parameter. Parameters for the Qz-K-feldspar sand mixture are derived from Montanari et al. (2017) and Del Ventisette et al. (2019). The parameters for the PDMS-Corundum mixture are derived from Maestrelli et al. (2020) at the experimental strain rate of the models.

[a]Internal friction coefficient (μ) corresponds to peak conditions, that is, the value reached at fault initiation (Montanari et al., 2017).

Specifically, the geometrical similarity (i.e., length and thickness) was achieved by setting a length or thickness scaling ratio (l^* and h^*, where the asterisk indicates the model to nature ratio) of 5×10^{-7}, such that 1 cm in the model corresponds to 20 km in nature. Models were run in normal gravity, so that the gravity scaling ratio g^* is equal to 1. The coefficient of internal friction (μ) requires to be similar both in the analog and natural material ($\mu^* \approx 1$), a condition fulfilled by the Qz-KFeld sand-mixture used in the experiments (Del Ventisette et al., 2019; Montanari et al., 2017). The density scaling ratio (ρ^*) is ~0.52, considering an average density of the brittle crust in nature of ~2,700 kg m^{-3} and leading to a stress scaling ratio ($\sigma^* = \rho^* g^* l^*$) of $\sim 2.6 \times 10^{-7}$. In order to obtain dynamic similarity, the cohesion scaling ratio (c^*) needs to be similar to σ^*. In our models, $c^* = 9.5 \times 10^{-7}$ and shares the same order of magnitude of σ^*, therefore satisfying this condition. The viscosity ratio (η^*), the strain rate ratio (ε^*) and the velocity ratio (V^*) are linked to the stress ratio (σ^*) by the relation:

$$\sigma^* = \eta^* \varepsilon^* = \eta^* (V^*/l^*) \quad (1)$$

Starting from the viscosity of the model Lower Crust $\eta_{LC} \approx 1.6 \times 10^5$ Pa s (calculated for the PDMS-corundum mixture following the procedure in Maestrelli et al. [2020]) and from the velocity of extension applied to the reference plate MP1 (10 mm/hr), a natural viscosity range for the lower continental crust of 10^{22}–10^{23} Pa s (e.g., Weijermars, 1997) corresponds to a calculated natural extension rate of $V_n \approx 1.1$–11 mm yr^{-1}, which is a plausible range for extension velocity at RRR junctions.

2.1.3. Monitoring of Deformation

To monitor model deformation, top-view photos were acquired with 30 s time intervals between the frames (using a Canon® EOS1100D camera). Furthermore, 3D perspective photos (Figure 1d) were taken (using a Canon® EOS1300D) at defined deformation intervals to perform photogrammetric analysis (e.g., Donnadieu et al., 2003; Schonberger & Frahm, 2016) and reconstruct Digital Elevation Models (DEMs) with the Agisoft Metashape® software. Specifically, for each model we built a DEM every 0.7 cm of incremental deformation (taking as reference the movement of MP1). The specific methodology and the parameters adopted for DEM reconstruction follow the standards detailed in Maestrelli et al. (2021a, 2021b). The resulting DEM resolution varies between a maximum of 0.13 mm/pix for Model SY-6 (obtained using 25 photos taken at 3.5 cm of incremental deformation)

Table 2
Analog and Numerical Modeling Parameters for the Two Experimental Series

Analog model name	Number of extensional stages	Velocity of MP1; v_{ref} (mm/h)	Velocity of MP2 and MP3, v (same for both) (mm/h)	Velocity ratio ($R = v_{ref}/v$)
Symmetric experimental Series (SY Series)				
A-SY-1	1	10	10	1
A-SY-2	2	10	10	1
A-SY-3	1	10	5	2
A-SY-4	2	10	5	2
A-SY-5	1	10	2.5	4
A-SY-6	2	10	2.5	4
Orthogonal experimental Series (OR Series)				
A-OR-1	1	10	10	1
A-OR-2	2	10	10	1
A-OR-3	1	10	5	2
A-OR-4	2	10	5	2
A-OR-5	1	10	2.5	4
A-OR-6	2	10	2.5	4

Numerical model name	Number of extensional stages	Velocity of MP1; v_{ref} (mm/yr)	Velocity of MP2 and MP3, v (same for both) (mm/yr)	Velocity ratio ($R = v_{ref}/v$)
Symmetric experimental Series (SY Series)				
N-SY-1	1	10	10	1
N-SY-2	2	10	10	1
Orthogonal experimental Series (OR Series)				
N-OR-5	1	10	2.5	4
N-OR-6	2	10	2.5	4

Note. The velocity of MP1 is kept constant and taken as a reference to calculate the R ratio. Notably, for numerical experiments, only the end-members were performed: models N-SY-1 and 2 (equivalent to analog models A-SY-1 and 2, respectively) and models N-OR-5 and 6 (corresponding to analog models A-OR-5 and 6).

and a minimum of 0.21 mm/pix for Model OR-4 (obtained using 14 photos acquired at 0.7 cm of incremental deformation).

2.2. Numerical Modeling

We used numerical forward models to explore the robustness of our experimental results. To this aim we conducted four numerical models—two single-stage and two two-stage models. Just like in the analog models, we systematically varied rate and direction of the extension velocity (Table 2). Numerical models were conducted using the finite element software ASPECT (Heister et al., 2017; Kronbichler et al., 2012; Rose et al., 2017), which solves the conservation equations of momentum, mass and energy for materials with visco-plastic rheology (Glerum et al., 2018). This software has previously been successfully applied to model rift tectonics, both in two (Heckenbach et al., 2021; Neuharth et al., 2022; Richter et al., 2021) and three dimensions (Corti et al., 2019; Glerum et al., 2020; Gouiza & Naliboff, 2021; Naliboff et al., 2020).

Our numerical model setup is similar to the analog experiments, albeit at natural scale. The model domain measures 153.6 × 179.2 × 38.4 km in x and y (horizontal) as well as z direction (vertical), respectively. The model comprises two material layers: Upper Crust of initially 20 km thickness with a density of 2,700 kg/m^3 and Lower Crust of 18.4 km thickness and a density of 2,850 kg/m^3. We refine the mesh toward the central domain of the model and achieve a minimum element size of 800 m within the region of interest. For reasons of numerical efficiency, we restrict the highest resolution to the upper crustal layer. Overall, the models solve for about 40

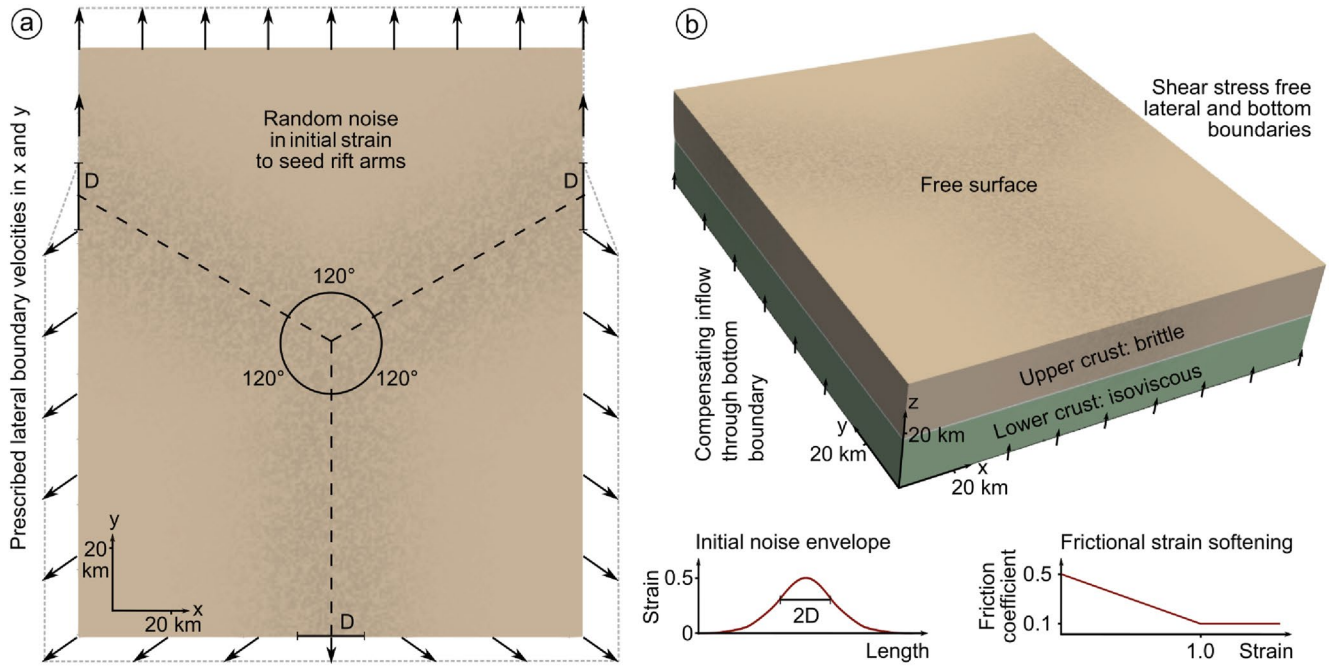

Figure 2. Numerical modeling setup. (a) Top view of 3D model illustrating the piece-wise linear velocity boundary conditions and the transition distance ($D = 20$ km) of boundary velocities. To initiate the three rift arms, we employ a random initial strain distribution (shown in dark), whose amplitude follows a bell-shaped curve with a standard deviation equal to D and a maximum strain of 0.5. We use frictional strain softening, where accumulated strain reduces the friction coefficient in a linear way until a critical strain of 1.0 is reached. For larger strains, the friction coefficient remains constant. (b) 3D view of numerical model showing the two-layer setup of a brittle upper crust and an isoviscous lower crust. Note that the numerical model is setup similarly to the analog models, albeit on natural scale. The major difference is that the triple junction geometry is imposed by lateral boundary conditions and initial condition, but not through a velocity pattern at the bottom boundary. See the main text for details.

million degrees of freedom per time step. Run on 12×96 CPUs for 24 hr, we compute 3 million years of tectonic evolution with 250 time steps of about 10–15 thousand years.

Similar to the laboratory experiments of this study, we assume purely brittle deformation in the upper crust and model isoviscous deformation within the Lower Crust. In particular, the employed rheologies are independent of temperature and strain rate. For the frictional layer, we use a cohesion of 5 MPa and a friction coefficient of 0.5 corresponding to a friction angle of 26.56°. The model involves frictional strain softening, such that we linearly reduce the friction coefficient by up to 80% for brittle strain between 0 and 1. For strains larger than 1 the friction coefficient remains constant. For the ductile layer, we employ a constant viscosity of 10^{20} Pa s.

In contrast to the analog experiments where divergence is induced through the motion of the three basal plates, extension in the numerical models is driven via prescribed lateral boundary conditions. This has the advantage that deformation is allowed to localize basin-ward, as the width of the deforming rift arms is not strictly imposed. That approach has however the disadvantage, that inherited weaknesses are required to initiate the 120° triple junction geometry. This is accomplished by means of a randomized bell-shaped initial strain pattern (Figure 2), which due to strain softening generates small-scale weaknesses mimicking inheritance within the brittle domain.

We employ velocity boundary conditions with a velocity of 10 mm per year (decreased to 2.5 mm per year for the R4 case, in line with analog model scaling), which falls in the range of plausible value of Rift-Rift-Rift junctions. Extension directions follow the characteristic rotational symmetry of triple junctions of 120°, except for the case of orthogonal extension between the two front plates (Table 2). At the bottom boundary, we prescribe a constant vertical inflow of material that balances the outflow through the lateral model sides. The top boundary constitutes a free surface (Rose et al., 2017).

2.3. Experimental Series

To investigate the evolution of the large-scale structural pattern at RRR triple junctions, we started from a simple and theoretical case in which the angle between the three rift branches and directions of extension are set at 120° (here after defined as the Symmetric experimental Series, SY Series; Figure 1e). We then also investigate the case in which the triple junction, despite conserving an angle of 120° between the three rift branches, develops under different extension directions (Orthogonal experimental Series, OR Series; Figure 1e). Specifically, models were differentiated depending on the number of extensional stages (single-stage or two-stage models) and by the Velocity Ratio (R), defined as:

$$R = \frac{v_{\text{ref}}}{v} \tag{2}$$

where v_{ref} is the velocity of the reference plate MP1 (always kept constant at 10 mm/hr for analog models and 10 mm/yr for numerical models) and v is the velocity of the moving plate MP2, which is equal to MP3 velocity (since the two plates are pulled by the same stepper motor). In two-stage models, only the reference plate MP1 moved (up to 2.1 cm) at the constant velocity of 10 mm/hr while the others were kept fixed during the first stage. All the three plates were then moved during the second stage, with velocity of MP2 and MP3 varying depending on the model (Table 2). Here below we provide details on how the two Series were developed. Both were conducted for analog and numerical models (labeled with letters "A" and "N," respectively). For the numerical models, only the end-member models were performed (see Table 2).

2.3.1. Symmetric Experimental Series (SY Series)

This experimental Series investigated the development of a geometrically symmetric RRR triple junction. The setup was designed with three rift branches trending at 120° from each other. The directions of extension are the bisector of the rift branches (i.e., trending at 120°) as shown in Figure 1e implying a symmetrical opening at the triple junction. Six models are shown in this experimental Series, differentiated according to the number of extensional stages (single-stage and two-stage models) and the ratio R. A single-stage and a two-stage model were run with $R = 1$. We then increased the R ratio up to $R = 4$, implying that for these models the velocities of MP2 and MP3 were a quarter of the MP1 velocity (Table 2).

2.3.2. Orthogonal Experimental Series (OR Series)

The orthogonal experimental Series differs from the SY Series in that an orthogonal extension was imposed to MP2 and MP3 (Figure 1e). All the other parameters were kept identical to the symmetrical models (Table 2). In this way we can compare the case of a non-symmetric extension occurring at a theoretical triple junction. We implemented this setup to test non-symmetric movement conditions between plates.

3. Modeling Results

Here we present analog and numerical models from the two experimental Series Experiments and have grouped and described them according to their R ratio and the number of stages (see Table 2). For simplicity, and to highlight differences between the two, we show together the equivalent analog models (same R ratio and number of deformation stages) from the SY Series and from the OR Series. The model pairs presented below therefore only differ in the orientation of extension direction for MP2 and MP3 ("symmetric" and "orthogonal" for SY models and OR models, respectively, Figure 1e). Models are described considering the topmost portion of the figure as the local north and the description of structural trends is given accordingly. Beside these, numerical models are shown together according to their R ratio and experimental Series (i.e., single and two-stage models with the same R value, both for SY and OR experimental Series) as they represent the selected end-members performed to be compared with their analog counterpart.

3.1. Analog Models

3.1.1. $R = 1$, Single-Stage Models: Models A-SY-1 and A-OR-1

Single-stage models A-SY-1 and A-OR-1 with $R = 1$ represent the standard experiments for each experimental Series. At time t_1 (Figure 3a) model A-SY-1 develops straight boundary faults, localized at the sides of the

10.1029/2022TC007491

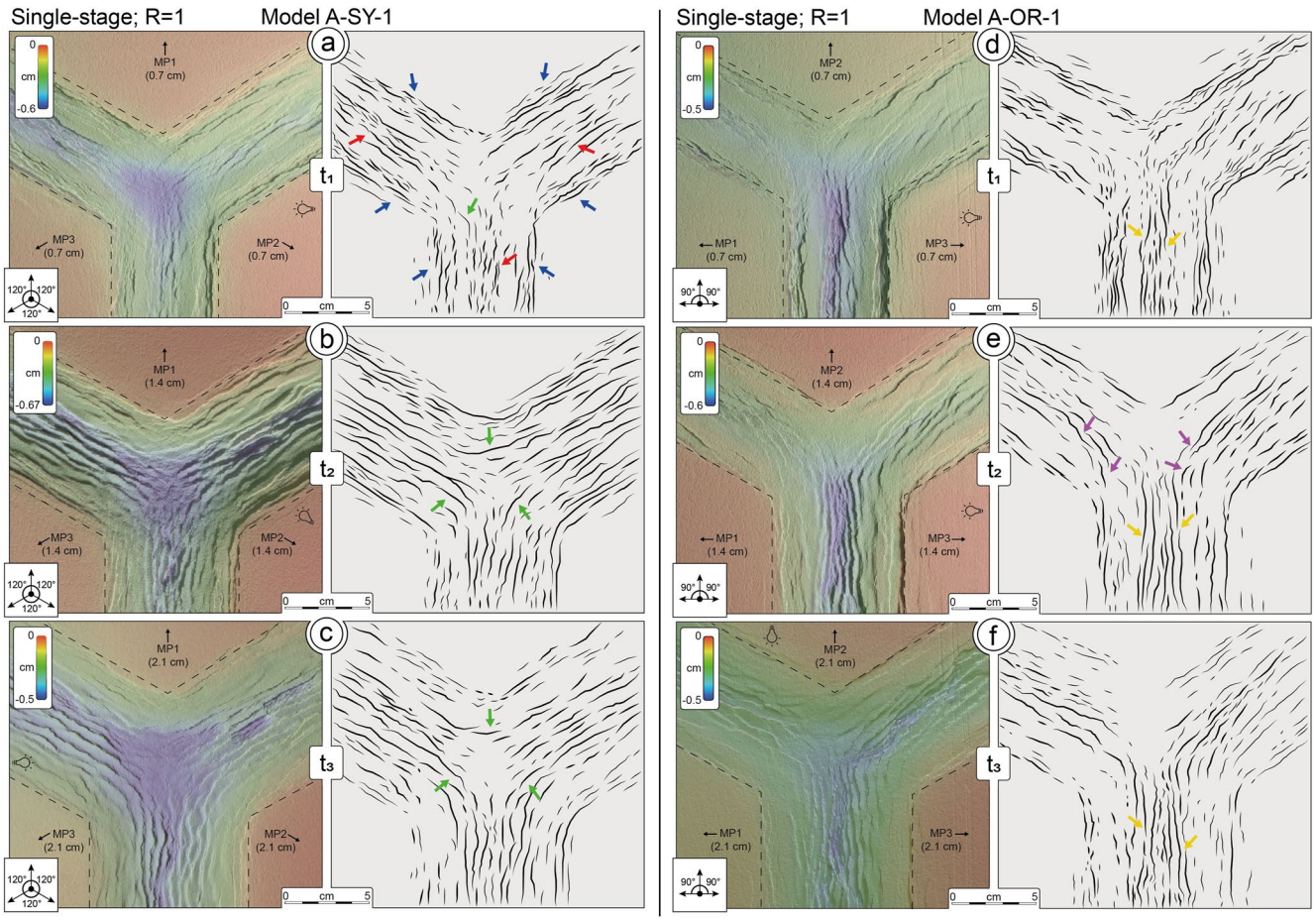

Figure 3. Single-stage models A-SY-1 and A-OR-1. (a–c) Three deformation steps (interval of 0.7 cm of deformation, taking as reference the movement of MP1) for model A-SY-1 (SY Series) shown as transparent DEMs superimposed onto top-view photos on the left-side panels, and as line-drawing on the right-side panels. Dashed lines on the left-side panels mark the approximate position of the moving plate edges below the model. Deformation interval t_3 shown in (c) corresponds to 2.1 cm of MP1 movement, that is, the end of deformation. (d–e) Model A-OR-1 (OR Series) illustrated as for Model A-SY-1. For the meaning of colored arrows refer to the text. Model A-SY-1 results in a markedly symmetrical fault pattern resulting from the symmetric extension conditions, while model A-OR-1, despite still largely symmetrical, reflects in its southern portion the effect of an orthogonal direction of extension.

stretching rubber sheet (blue arrows in Figure 3a). Contemporaneously, a series of intra-rift (or axial) sub-parallel faults with millimetric displacement nucleate (red arrows). Toward the central area, this model develops curvilinear faults, symmetrically linking the boundary faults from the three rift branches (green arrow). Similarly, curvilinear faults bound and contribute to strain in the central area, which becomes the locus of maximum subsidence since time t_1 (Figure 3a) and for progressive deformation (time t_2 and t_3, Figures 3b and 3c; green arrows). The last stage of deformation (t_3, Figure 3c) shows a perfectly symmetric triple junction, while the comparison between time steps t_1 to t_3 indicates that the locus of maximum subsidence remains centered (see Appendix A, Figure A1). Contrarily, model A-OR-1, despite bearing the same R ratio, reflects the asymmetric stress field conditions imposed by the E-W trending extension for MP2 and MP3 (Figure 1e). This results in marked narrow area of N-S trending faults in the southern rift branch (orange arrows) and curvilinear en-echelon structures, particularly evident at t_2 (Figure 3e; violet arrows), connecting this branch with the other two.

3.1.2. $R = 1$, Two-Stage Models: Models A-SY-2 and A-OR-2

Models A-SY-2 and A-OR-2 were set with $R = 1$ but differ from models A-SY-1 and A-OR-1 in that two extensional stages were imposed to the former. Figure 4a shows Model A-SY-2 after the three steps of deformation occurred during the first stage (i.e., t_3; time steps t_1 and t_2 are not shown). At time t_3 this model shows en-echelon structures bounding axial grabens (blue arrows in Figure 4a) and connecting the northwestern and northeastern rift branches. During the second stage of deformation (Figures 4b and 4c), when all the three plates move, a

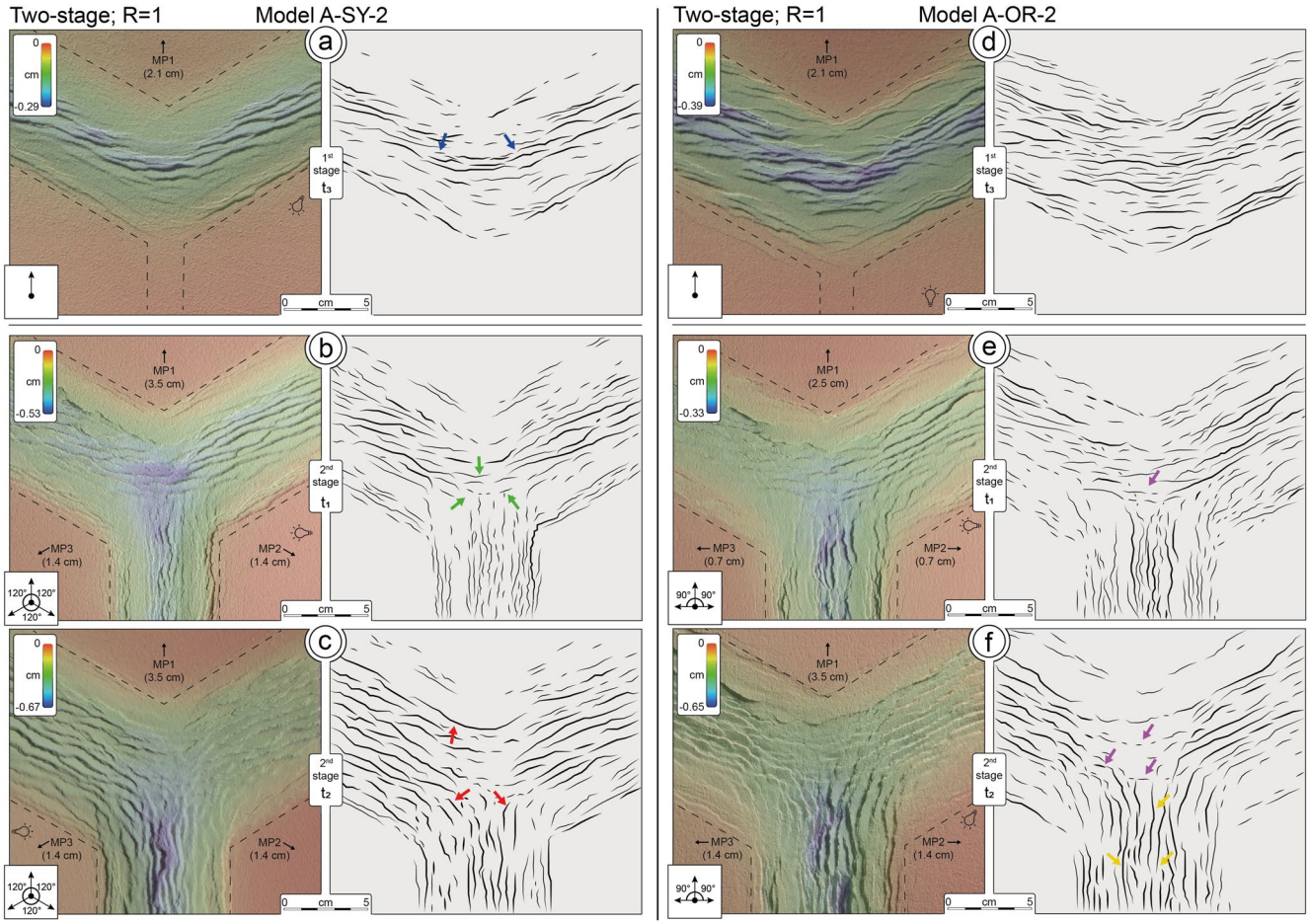

Figure 4. Two-stage models A-SY-2 and A-OR-2. (a) The end of the first stage of deformation for model A-SY-2 (SY Series), after 2.1 cm of MP1 movement. (b and c) The two deformation steps (interval of 0.7 cm of deformation, taking as reference the movement of MP1) occurring during the second deformation stage for model A-SY-2. The two models are illustrated as in Figure 3. Deformation interval t_2 shown in (c) corresponds to a total of 3.5 cm of MP1 movement (2.1 cm acquired during the first stage and 1.4 during second stage), that is, the end of the deformation. (d and e) Model A-OR-2 (OR Series) illustrated as for Model A-SY-1: (d) corresponds to the end of the first stage of deformation, while (f) shows the model at the end of the second stage (i.e., end of deformation). For the meaning of colored arrows refer to the text. Both models show the presence of inherited E-W trending faults interacting with N-S trending fault developed during the second stage of extension. Nonetheless, both models tend to reacquire symmetry as the second stage of extension proceeds.

symmetric stress field is re-established, and the conditions tend to those of model A-SY-1, with newly formed curvilinear faults developing and connecting the three rift branches (red arrows in Figure 4c). Nonetheless, at time t_2 (Figure 4c) the model, showing an overall symmetry, still presents inherited and reactivated E-W trending faults located in the southern portion of the triple junction, relics of the first stage of deformation (green arrows in Figure 4b). Similarly to model A-SY-2, model A-OR-2 (Figures 4d–4f) shows a less symmetric triple junction, with E-W trending faults inherited from the first stage (violet arrows in Figures 4e and 4f). Furthermore, as it occurs in model A-OR-1, the southern rift branch is markedly more developed, with a pattern of laterally continuous faults resulting from the orthogonal extension imposed between MP2 and MP3 (orange arrows in Figure 4f). In both models, the area of maximum subsidence is located close to the intersection between the southern rift branch and the other two branches (Figure A2 in Appendix A).

3.1.3. $R = 2$, Single-Stage Models: Models A-SY-3 and A-OR-3

Single-stage models A-SY-3 and A-OR-3 are set with $R = 2$. This entails, in model A-SY-3 (Figures 5a–5c), the development of a northeastern and northwestern symmetric rift branches (with similar subsidence) but a slightly less developed southern breach, as a result of the decreased component of extension velocity acting between MP2 and MP3. Internal or axial faults are mostly rectilinear with almost no right or left stepping components (blue arrows in Figures 5a–5c). The curvilinear pattern for boundary faults is observable also in this model (red

10.1029/2022TC007491

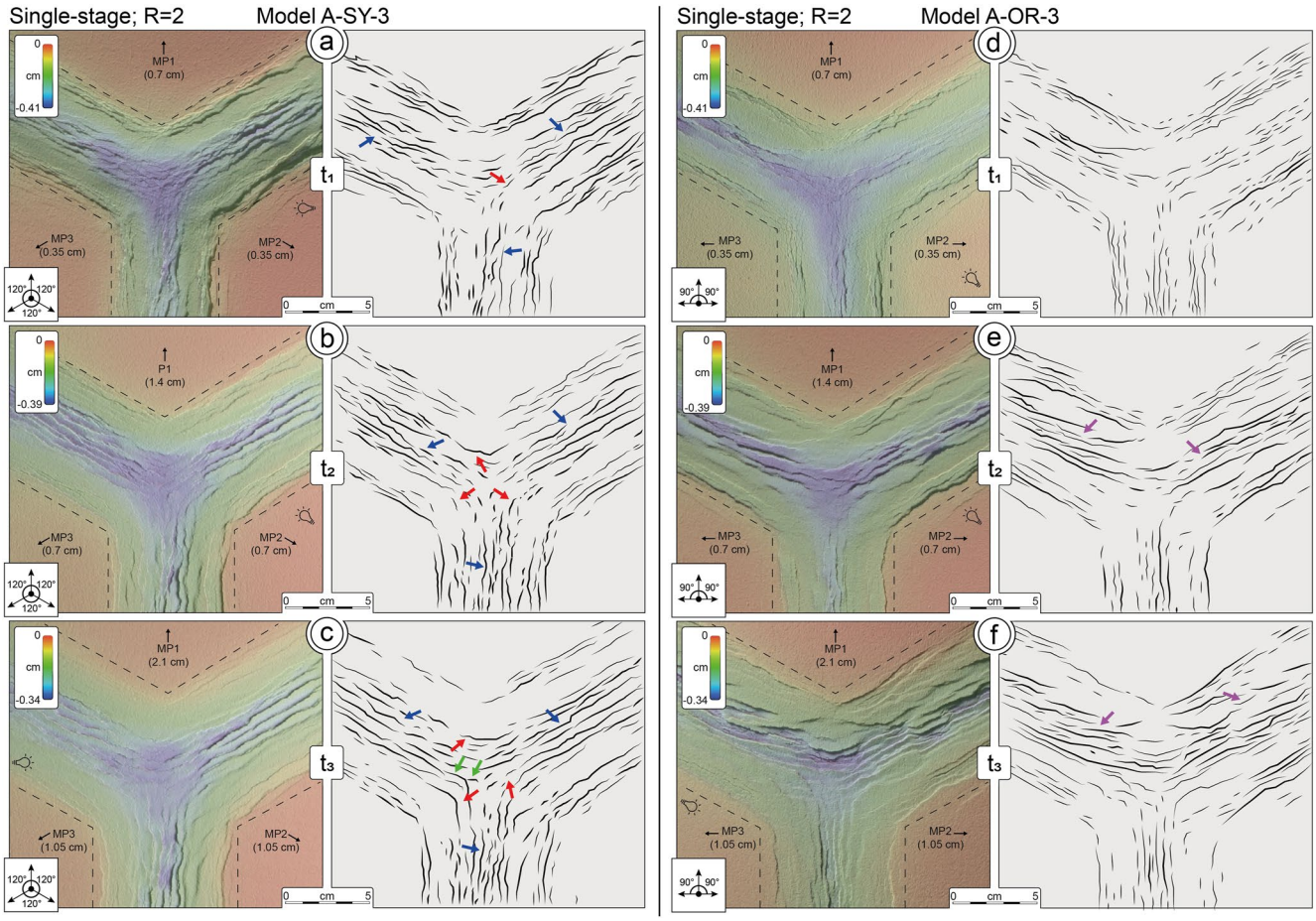

Figure 5. Single-stage models A-SY-3 and A-OR-3 run with $R = 2$ belonging to SY and OR Series, respectively. Models are illustrated as in Figure 3. Both models show high-angle fault interaction resulting from the effect of an increased R ratio, which also implies a less developed southern rift branch. For the meaning of colored arrows refer to the text. In model A-SY-3, axial faults are mostly rectilinear while the curvilinear pattern for boundary faults is still observable, despite it interacts with E-W trending faults. Model A-OR-3 shows a similar evolution but developed a marked en-echelon fault pattern in the northeastern and northwestern rift branches deriving from the orthogonal extension imposed on the southern rift branch.

arrows in Figures 5a–5c), yet less marked and interacting with an E-W trending fault pattern crosscutting the triple junction area (more evident at time t_3; Figure 5c, green arrows) and resulting from the higher (relative) northward velocity component associated with the movement of MP1. Model A-OR-3 (Figures 5d–5f) shares a similar evolution, but developed a marked en-echelon fault pattern in the northeastern and northwestern rift branches (violet arrows in Figures 5e and 5f), as a result of the asymmetric stress field induced by the orthogonal extension occurring in the rift branch formed between MP2 and MP3 and the higher obliquity of the northern rift branches. This latter branch, similarly to model A-SY-3, is less developed than the other two branches, as a result of the velocity conditions imposed by the R ratio. Both models show at the end of deformation (t_3) an area of maximum subsidence located in a more northern position than in single-stage models with $R = 1$ (see Appendix A, Figure A1).

3.1.4. $R = 2$, Two-Stage Models: Models A-SY-4 and A-OR-4

In models A-SY-4 and A-OR-4, the development of E-W trending faults and the overall asymmetry associated with the $R = 2$ ratio is increased by the occurrence of two extensional stages. After the end of the first stage, both models A-SY-4 (Figure 6a) and A-OR-4 (Figure 6d) show marked en-echelon, left- and right-stepping faults both at the boundaries and in the axial area (blue arrows in Figures 6a and 6d). As the second stage reaches time t_1 (Figures 6b and 6e) the two models have developed N-S trending faults in the southern rift branch (red arrows in Figures 6b, 6c, 6e, and 6f), resulting in high-angle fault interaction at the junction between this latter branch and the other two (green arrows in Figures 6b, 6c, and 6f). Curvilinear boundary faults linking the three rift branches

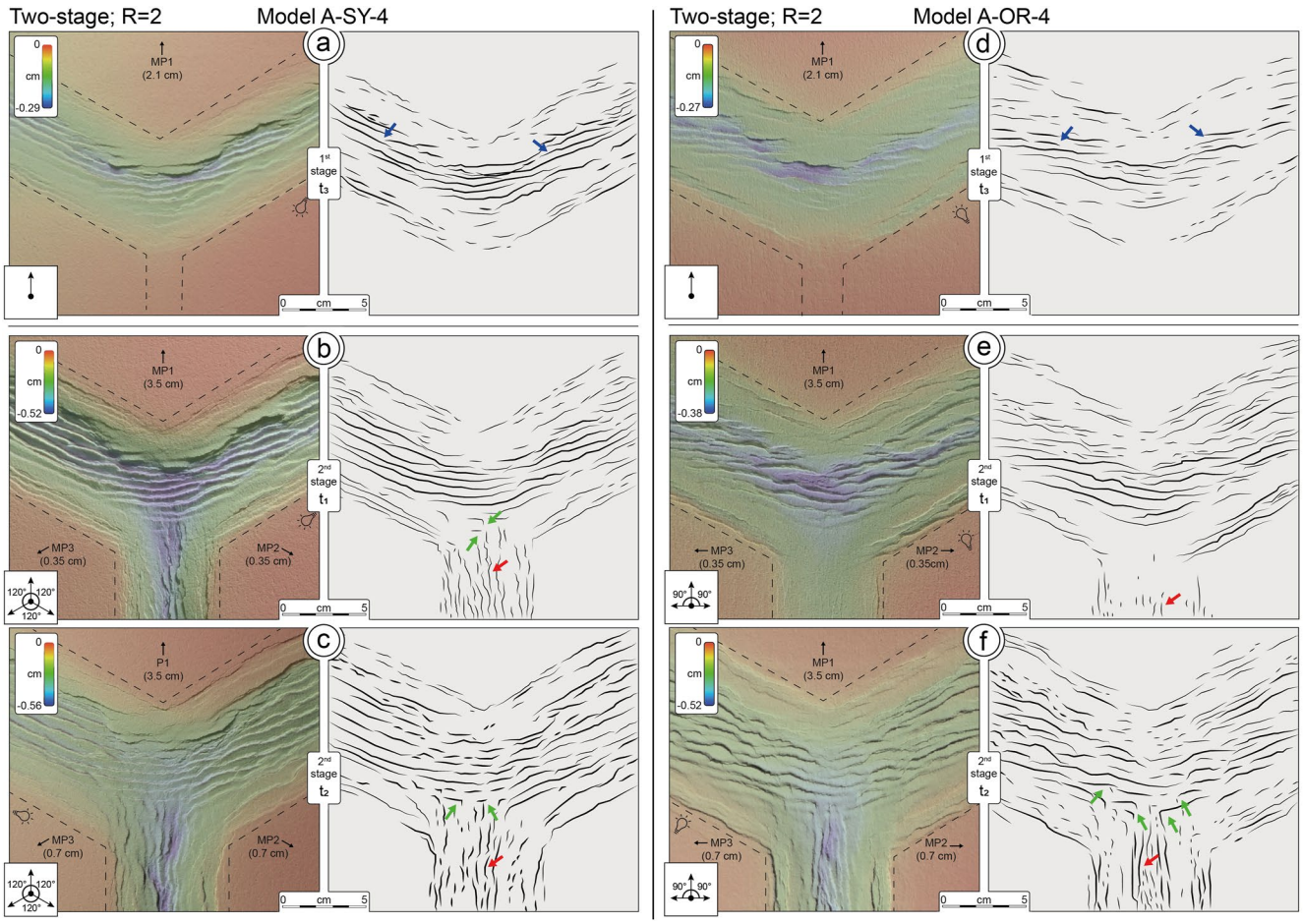

Figure 6. Two-stage models A-SY-4 and A-OR-4 run with $R = 2$. Belonging to SY and OR Series, respectively. Models are illustrated as in Figure 3. The two extensional stages induce in both models a marked high-angle fault interaction at the triple junction location. This is enhanced in model A-OR-4 by the orthogonal extension responsible for the development of the southern rift branch. Refer to text for the meaning of colored arrows.

observed in the previously described models are here missing. This is particularly evident in both models at the end of the deformation (t_2 of second stage; Figures 6c and 6f). Finally, the area of maximum subsidence remains located in the southern position in both models at the end of deformation (see Appendix A, Figure A2).

3.1.5. $R = 4$, Single-Stage Models: Models A-SY-5 and A-OR-5

Models A-SY-5 and A-OR-5 experience asymmetric conditions induced by strong differential velocities. This results in markedly developed northeastern and northwestern rift branches at time step t_1 (Figures 7a and 7d), contrary to the southern branch, which remains less developed and is defined by shorter and less continuous faults than those of models with $R < 4$ (blue arrows in Figures 7c and 7f). While at the end of the deformation (time step t_3; Figure 7c) model A-SY-5 mostly shows rectilinear faults, and the presence of en-echelon structures is limited to the central area of the triple junction, in model A-OR-6 en-echelon and right/left-stepping faults are widespread in all rift branches (red arrows in Figures 7c and 7f), as a result of the coupled effect of asymmetric extension directions and velocity conditions (i.e., $R = 4$). Nonetheless, in both models high-angle fault interaction is visible at the southern limit of the triple junction (green arrows in Figures 7c and 7f). Finally, in both models, the maximum subsidence is located more northward than equivalent models with $R = 2$ (i.e., models A-SY-3 and A-OR-3; see Figure A1 in Appendix A).

3.1.6. $R = 4$, Two-Stage Models: Models A-SY-6 and A-OR-6

Two-stage models A-SY-6 (Figures 7d–7f and Figures 8a–8c) and A-OR-6, represent asymmetric end-members as they experience the two stages of extension coupled with the highest R ratio (i.e., $R = 4$). This condition takes

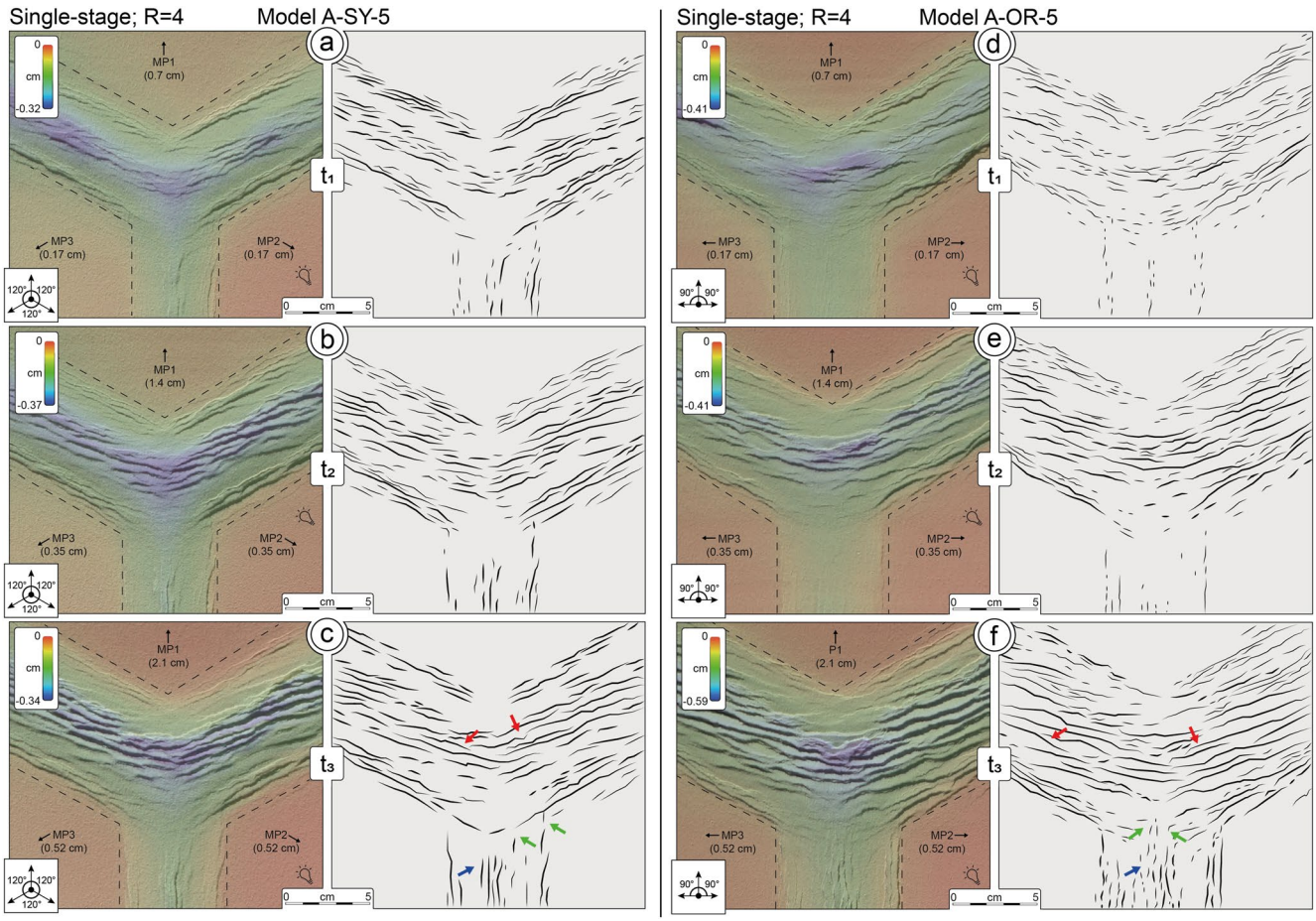

Figure 7. Single-stage models A-SY-5 and A-OR-5 run with $R = 4$ belonging to SY and OR Series, respectively. Models are illustrated as in Figure 3. High R ratio value induces in both models a reduced development of the southern rift branch; nonetheless, high-angle fault interaction is still visible in both models at the triple junction location. For the meaning of colored arrows refer to the text.

to extremes the consideration outlined from models A-SY-5 and A-OR-5, as the occurrence of two distinct stages of deformation increase the effect of two separated stress fields, which ultimately lead to a marked high-angle fault interaction (blue arrows in Figures 8b–8d and 8f) at the southern limit of the triple junction area and a less developed southern rift branch (red arrows in Figures 8c and 8f). In this case, the position of the triple junction does not correspond to the location of the maximum subsidence (Figure A2 in Appendix A). Notably, in model A-OR-6, NS-trending faults associated with the opening of the southern rift branch experience a more efficient northward propagation, crosscutting and interacting with relict faults inherited from the first stage of deformation. Finally, as in the case of model A-SY-6, the area of maximum subsidence is located northward of the triple junction (Figure A2 in Appendix A).

3.2. Numerical Models

Numerical models were run to be compared with their analog counterpart. Consequently, the following two sections summarize numerical models in relation to respective analog models.

3.2.1. $R = 1$, Single and Two-Stage Models, Symmetric Series: Models N-SY-1 and N-SY-2

These two numerical models, belonging to the Symmetric experimental Series, where run with similar setup to analog models A-SY-1 and 2, respectively. They therefore represent the two symmetric end-members (single- and two-stage). Model N-SY-1 (Figures 9a–9c) well reproduces the symmetric fault pattern observed in the equivalent analog model (cf., Figures 3a–3c), with three symmetric rift branches and curvilinear faults, linking the structures propagating from one branch to another (Figures 9b and 9c, red arrows). Interestingly, also in the

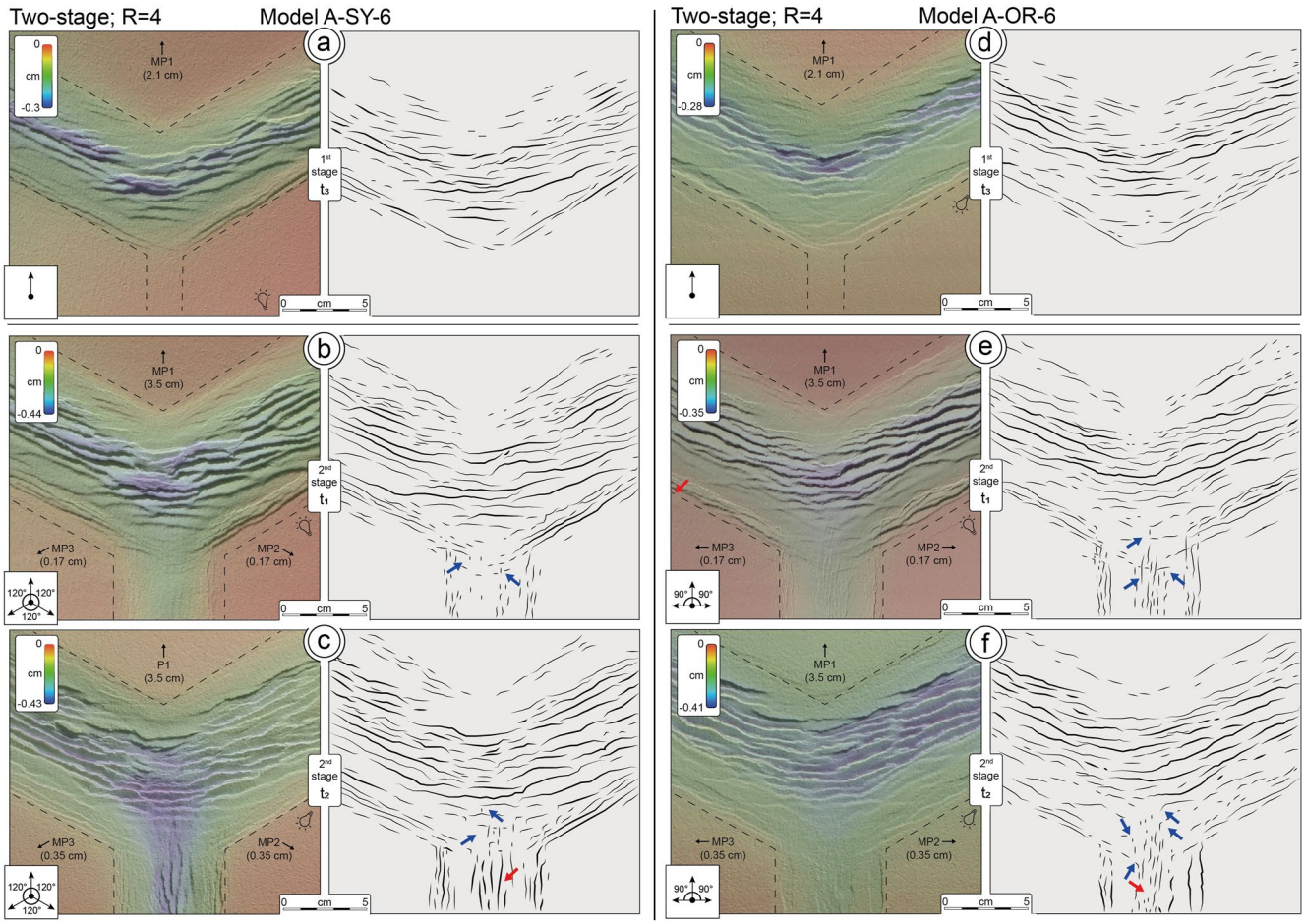

Figure 8. Two-stage models A-SY-6 and A-OR-6 run with $R = 4$. Belonging to SY and OR Series, respectively. Models are illustrated as in Figure 3. The coupled effect of a high R ratio with two extensional stages induces in these models a marked high-angle fault interaction at the triple junction location, which results strongly asymmetric. Refer to text for the meaning of colored arrows.

numerical model, the area of maximum subsidence remains located at the center of the interacting fault pattern. Model N-SY-2 reflects the effect of the two stages of deformation, resulting in a less symmetric fault pattern with some high-angle fault interaction (Figures 9e and 9f; green arrows). This characteristic is also present in the analog models A-SY-2, with this effect being more visible during the incipient stages of the deformation of the second stage. This effect is afterward mitigated by the deactivation of the asymmetric stress field imposed during the first-stage, once a symmetric stress filed was re-established during the second stage. In this numerical model, E-W trending faults remain better visible and resulted in the more evident high-angle fault interaction. Nonetheless, the $R = 1$ setup induces an overall symmetric architecture, with the three rift branches bearing approximately the same width and the same gradient of deformation as in analog models A-SY-2.

3.2.2. $R = 4$, Single and Two-Stage Models, Orthogonal Series: Models N-OR-5 and N-OR-6

These numerical models, belonging to the Orthogonal experimental Series exhibit good agreement with their equivalent analog models A-OR-5 and 6. With high R ratio ($R = 4$) and orthogonal extension imposed on the southern rift branch, they represent the most asymmetric models out of all the experiments. Model N-OR-5 (Figures 10a–10c; single-stage) shows a marked high-angle fault pattern where the southern rift branch interacts with the others (Figure 10c, red arrows), similarly to what is observed in analog model A-OR-5, with the single-stage of deformation not sufficient to maintain a symmetric triple junction, and the orthogonal extension coupled with the high R value leading to a strongly asymmetric fault pattern. Strong asymmetry occurs also in model N-OR-6 (Figures 10d–10f), where the two stages of deformation show the extreme in fault interaction occurring from the northward propagation of the less-developed southern rift branch (green arrows), as observed

10.1029/2022TC007491

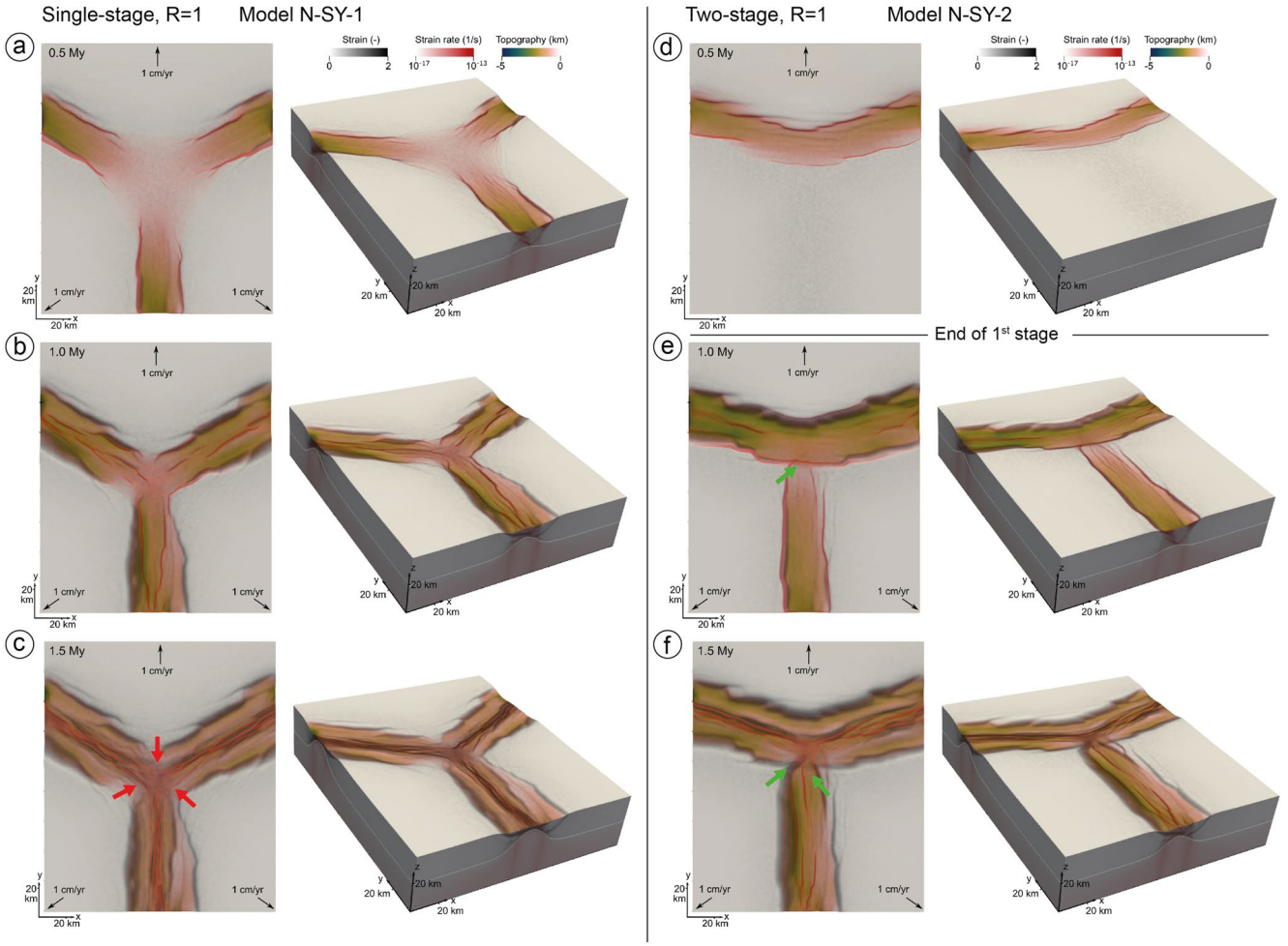

Figure 9. Single and two-stage models (a–c) N-SY-1 and (d–f) N-SY-2, run for the symmetrical Series. Compare to analog models A-SY-1 and A-SY-2 (Figures 3a–3c and Figures 4a–4c), respectively: model N-SY-1 well reproduces the symmetric fault pattern observed in model A-SY-1, with three symmetric rift branches and curvilinear faults. Besides, model N-SY-2 results in a less symmetric fault pattern with some high-angle fault interaction, as occurring in the analog models A-SY-2. Refer to text for the meaning of colored arrows.

in analog model A-OR-6. Notably, also in the case of the numerical model N-OR-6, the NS-trending faults induced by the orthogonal extension on the southern rift branch experience a more efficient propagation, cross-cutting the relict faults inherited from the first stage of deformation and are therefore similar to the observations made for the analog model. In contrast to the analog models, the rift arms of the numerical models are not fixed by a basal velocity boundary condition. This leads to a marked difference in large-scale rift geometries such that models with a large velocity ration ($R = 4$) feature a high angle between rifts arms bounding the fast plate in the north. The occurrence of this almost T-shaped Rift-Rift-Rift geometry can be understood through a mechanical argument (Gerya & Burov, 2018): faster rifts dissipate more work so that the overall work can be minimized when the slow rift branch is longer while the fast rift branches are shorter.

4. Discussion

Our analog and numerical models are amongst the first to specifically explore the structural evolution of Rift-Rift-Rift triple junctions. In particular, our analog models are the first to reproduce the contemporaneous motion of three plates. A range of previous analog models have focused on the dynamics of the triple junctions at various scales (e.g., Khalil et al., 2020, 2021; Oliveira et al., 2021; Souriot & Brun, 1992). In contrast to our models, however, they focused on two-plate divergent tectonic systems. This limits the degree to which our results can be compared. Nevertheless, we discuss specific similarities and differences when comparing results to the natural

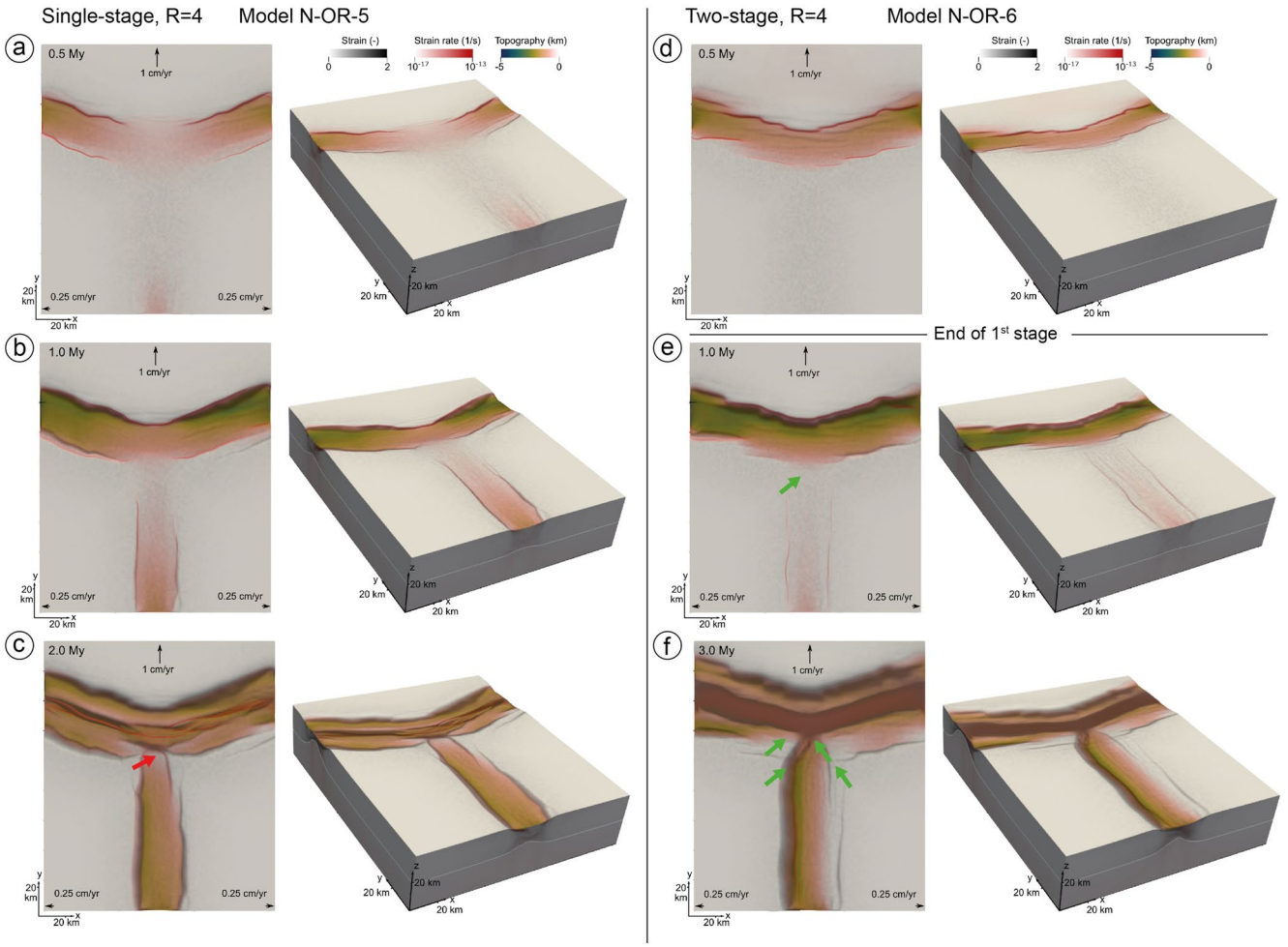

Figure 10. Single and two-stage models (a–c) N-OR-5 and (d–f) N-OR-6, run for the asymmetrical Series. Compare to analog models A-OR-5 and A-OR-6 (Figures 7d–7f and Figures 8d–8f), respectively: model N-OR-5 shows a marked high-angle fault pattern at the intersection between the southern rift branch and the others, similarly to analog model A-OR-5. In model N-OR-6, the two stages of deformation induce fault interaction occurring from the northward propagation of the southern rift branch, as in analog model A-OR-6. Furthermore, NS-trending faults induced by the orthogonal extension on the southern rift branch experience a more efficient propagation and crosscut the inherited faults from the first stage. For the meaning of colored arrows refer to the text.

case of the Afar triple junction. Khalil et al. (2020, 2021) in fact, performed lithospheric-scale analog models to specifically reproduce the conditions acting at the Afar triple junction. Their setup involved the movement of two plates only, but also considered the effect of mechanical weakening induced by mantle plume-related anomalies. Despite the different setup, our observations are in line with their outcomes on the Afar triple junctions and will be specifically discussed in Section 4.5.

Concerning numerical models, a few works simulated the interaction between RRR triple junction and mantle plumes, testing the specific role of plumes on broad strain evolution and providing information on the crustal and asthenosphere dynamics, rather than focusing on the surface structural architecture, while others mainly focused on the understanding of magma paths below triple junctions and the role of mantle plumes (e.g., Dordevic & Georgen, 2016; Georgen & Lin, 2002; Karaoğlu et al., 2016; Koptev et al., 2018), therefore without investigating the structural patter evolution, as our models do. Other works demonstrated that transient quadruple and triple junctions formed by continental breakup, are gradually converted into stable oceanic triple junctions (Gerya & Burov, 2018). Gerya and Burov (2018) documented, in agreement with our models, how the geometry of triple oceanic junctions may vary from strongly asymmetrical T-junctions to ideal 120° junctions. Interestingly, they also document the important role of differential plate velocities on the architecture of the resulting triple junction. However, Gerya and Burov (2018) analyzed Ridge-Ridge-Ridge systems with development of new oceanic crust, whereas our models reproduced a continental rifting stage before the break-up of the continental lithosphere

(i.e., Rift-Rift-Rift junctions). These two processes (Ridge-Ridge-Ridge vs. Rift-Rift-Rift) systems are driven by different physics, and therefore some caution is required when comparing these different modeling approaches. Nonetheless, if we consider our analog and numerical single-stage models, rift obliquity seems to be controlled by the R ratio (i.e., differential plate velocity), therefore matching with their evidence suggesting the formation of non-orthogonal (with respect to the direction of extension) ridges. In our models, rifts are orthogonally extending only if $R = 1$ (i.e., plates velocity is uniform), therefore matching the McKenzie and Morgan (1969) model only in the specific case of symmetric, single-stage end-member, for which, we also do not observe triple junction migration with time (see Section 4.4), as suggested by these authors.

4.1. Modeling Limitations

Before comparing suitable models to observations from the Afar triple junction, it is worth mentioning some limitations of our analog and numerical models. For what concerns analog models, beyond the common limitations affecting the methodology (e.g., Schellart & Strak, 2016), a consideration is that they approximate complex thermo-mechanical processes associated with rifting (such as rift—plume interactions) with purely mechanical processes. This implies that no effect of thermal or magmatic weakening is reproduced and no plume impingement is simulated in our models. The role of these processes on the initiation of continental rifting is debated (e.g., Burke & Dewey, 1973; Stein et al., 2022 and reference therein) and should be kept in mind when interpreting our models. The same assumption (and hence limitation) applies to the numerical ones, in which temperature effects are not implemented. A final consideration on our setup can be done on the triple junction geometry: for reasons of simplicity, we chose to implement a 120° junction. This obviously represents a limitation that can be overcome by designing different configurations in future triple junction setups, likely shedding light on specific natural cases.

4.2. Triple Junction Definition and Geometry

The interaction between three rift branches creates a complex and time-dependent deformation field, which allows at least for three ways of defining the location of a triple junction: specifically, our models show patterns of interacting faults in the area where the three rift branches connect. We can therefore define a first type of triple junction (a) as the area where faults related to the different motion of the three moving plates interact. The above definition, which is used throughout this manuscript is based on the interpretation of fault structures and we therefore suggest to call it "structural triple junction." (b) An alternative definition can be constructed based on large-scale plate kinematic considerations. Such a "kinematic triple junction" is often used for describing the evolution of ridge-ridge-ridge interactions. Its motion has been defined geometrically in velocity space as the circumcenter of the triangle consisting of individual plate velocities (McKenzie & Morgan, 1969) and an alternative definition for a "kinematic triple junction" employing a work minimization principle has been proposed by Gerya and Burov (2018). (c) Yet another tentative definition may relate to the location of minimum surface topography that is clearly visible in almost all our models and that would tend to attract the deposition of sediments or lava flows (see Appendix A, Figures A1 and A2). We note that such a "depositional triple junction" is closely related to thinning and associated isostatic subsidence.

Focusing on the structural triple junction definition, in the symmetric analog and numerical models, A-SY-1 and N-SY-1(Figures 3a–3c and 9a–9c), this area corresponds to a perfectly symmetric "Y-shaped" fault interaction, related to the propagation of the curvilinear faults from the three different branches. In most of our models, instead, the triple junction corresponds to the area where N-S trending faults propagating northward from the southern rift branch intersect or interact with E-W trending faults associated with the northward motion of MP1. The location of this interaction depends on the modeling conditions, that is, the value of the R ratio, the symmetric or asymmetric extension and the influence of a single or two stages of deformation. Opposite to the symmetric model A-SY-1, we observe that the asymmetric models A-OR-6 and N-OR-6 (Figures 8d–8f and 10d–10f), in which the high R ratio ($R = 4$) coupled with the orthogonal extension occurring in the southern rift branch and with the two extensional stages, lead to a marked high-angle interaction in the southern boundary of the central area, defining the location of the triple junction. This type of fault interaction defines a "T-shaped" geometry representing the asymmetric end-member for our experimental Series (Figures 11a and 11d). The other models, define intermediate geometrical interactions, closer to the Y-shaped pattern in the case of models set with high R ratios and/or a single-stage of deformation and/or symmetrical extension. For example, despite the presence

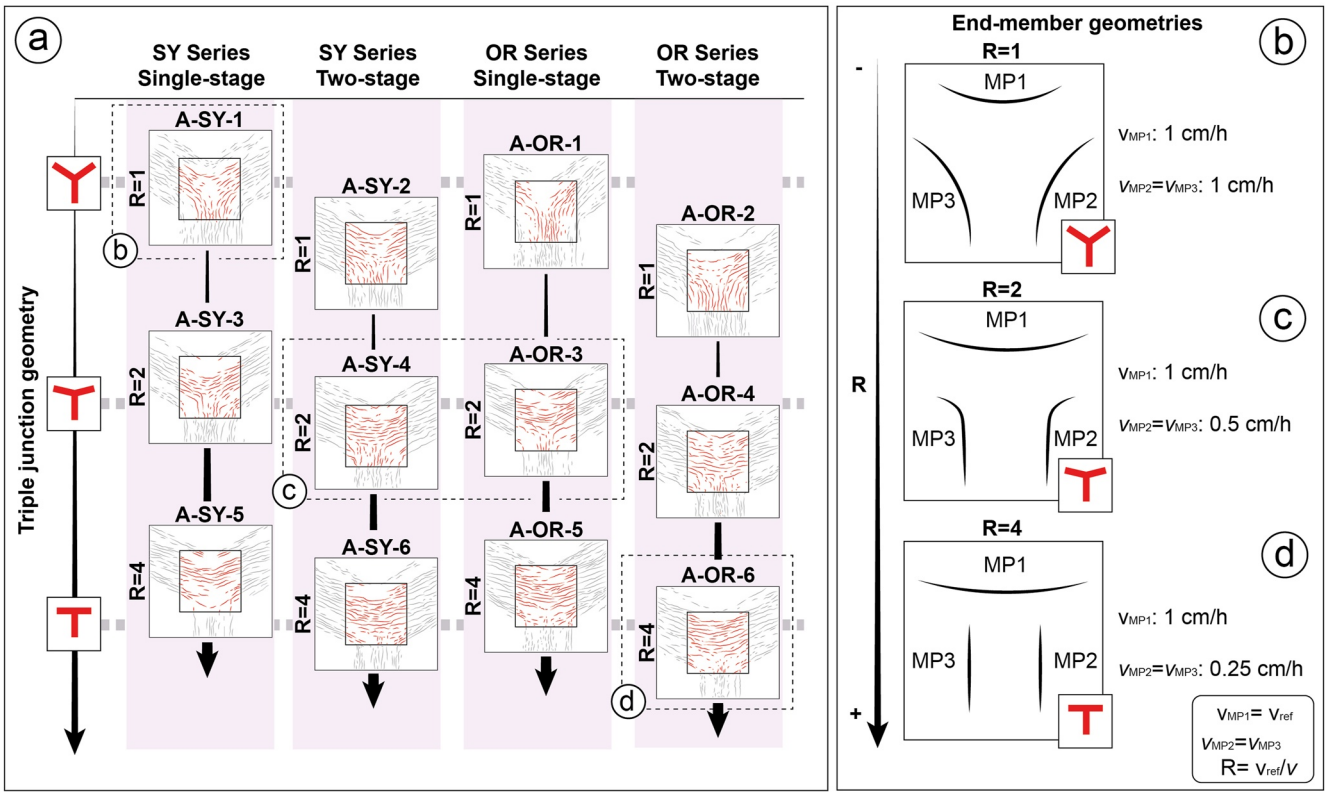

Figure 11. Sketch illustrating the end-member geometries for the fault pattern of the extensional triple junction obtained in analog models. End-members are defined observing fault interaction at the triple junction location. (a) Schematic chart illustrating the variation of triple junction fault pattern as a function of the *R* value, number of stages and direction of extension (i.e., SY and OR Series). As the *R* ratio increases the models shift from a symmetrical "Y-shaped" fault pattern ($R = 1$) toward an asymmetrical "T-shaped" fault patter ($R = 4$). This effect is coupled with those of the two other parameters: two stages of extension and orthogonal extension contribute the occurrence of a T-shaped fault pattern while single-stage models under symmetrical extension produces Y-shaped triple junctions. Intermediate conditions lead to intermediate geometries. (b–d) Sketch illustrating fault geometries of the two end-members (a and d) and the intermediate condition (c). Note that the case illustrated in (c) can also be applied to models A-SY-3 and A-OR-4 (with $R = 2$) in addition to models A-SY-4 and A-OR-3.

of two deformation stages, models A-SY-2 and N-SY-2 (Figures 4a–4c) show a fault pattern rather similar to models A-SY-1 and N-SY-1 (Figures 11a and 11b), in response to a low *R* ratio ($R = 1$) and symmetric extensional conditions. Besides, models A-SY-5 and N-SY-6, despite the single deformation stage and the symmetric direction of extension, show a high-angle fault pattern like those occurring in models A-OR-6 and N-OR-S, as a result of high *R* value ($R = 4$). The same reasoning, with opposite outcomes, can be applied to models A-SY-5 and A-SY-6 for the SY Series, and models A-OR-1 and A-OR-2 for the OR Series (Figure 11a). All other models define an intermediate geometry halfway between the Y-shaped and T-shaped geometries, experiencing hybrid modeling conditions (single of two-stage models belonging to both SY and OR Series with intermediate $R = 2$ ratio; Figures 11a and 11c). This suggests that the *R* ratio, that is, the relative velocity of plate motion exerts a stronger influence on triple junction geometry than the conditions associated with the direction of extension and the presence of one/two extensional stages.

We also measure the topography of our models, which shows that the depositional triple junction (i.e., the area of maximum subsidence) often does not correspond with (and is generally located northward of) the high-angle fault interaction defining the triple junction location, as described in detail in Appendix A (Figures A1 and A2). This discrepancy is associated with the strong control exerted by the velocity ratio *R* on the depocenter, while triple junction position reflects the coupled effect of the three investigated parameters. Furthermore, the location of the maximum subsidence experiences a northward migration with increasing *R* ratio values throughout the models. This reflects the crustal stretching associated with the dominant effect of the northward velocity component of MP1 with respect to the other two MPs, and the resultant area of maximum subsidence is centered at the intersection of the three rift branches only in the case of Y-shaped models as a result of the symmetric conditions of extension (Figures A1 and A2).

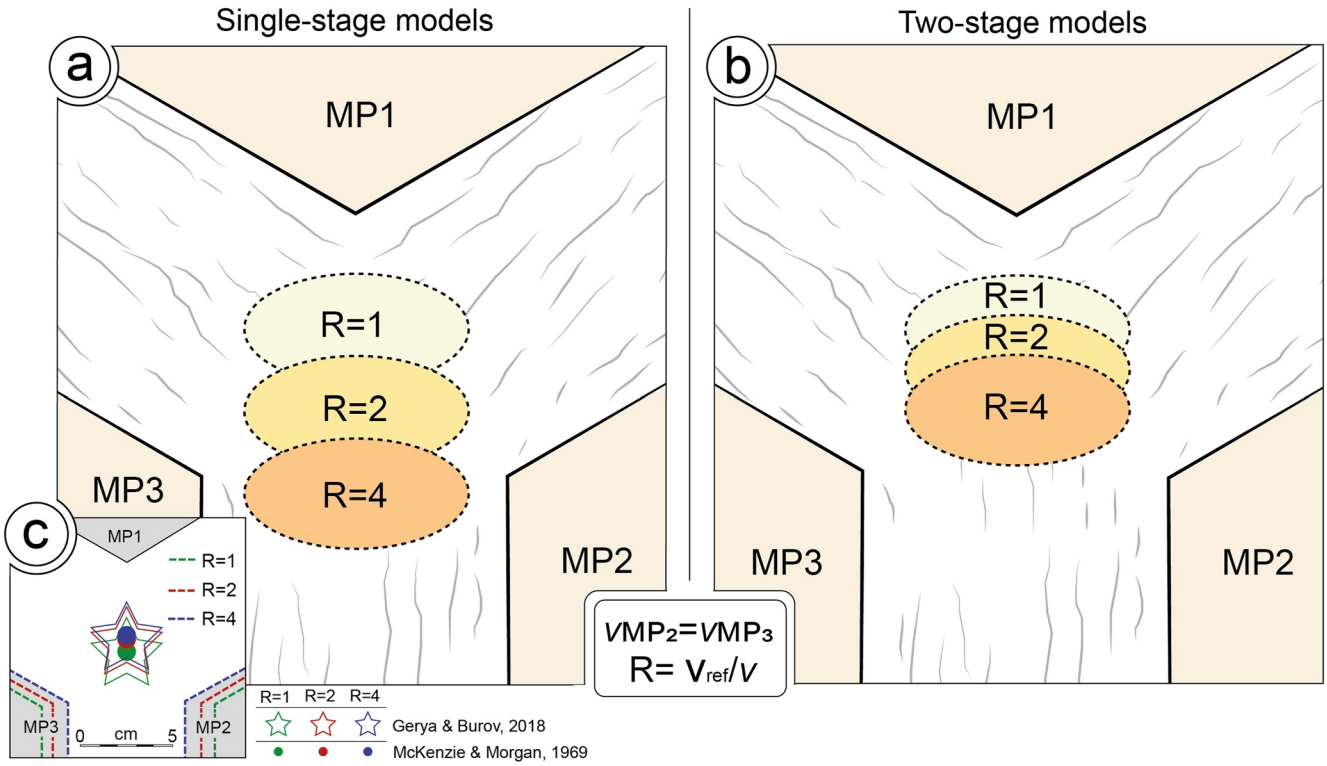

Figure 12. Schematic sketch illustrating the structural triple junction position depending on *R* value. (a) As *R* increases, the triple junction locates southward in single-stage models. This trend is similarly (but less markedly) observed in two-stage models (b), as *R* value increases. (c) For comparison, we plot the location of the kinematic triple junction as computed from the models of McKenzie and Morgan (1969) (stars) and Gerya and Burov (2018) (circles) as a function of the *R* values for single-stage models from SY Series. The dashed colored lines indicate the relative position of the MP2 and MP3 edges with different *R* ratios. The position of MP1, moving at the same velocity in all the models, is taken as reference. Notably, opposite to the structural triple junction, the kinematic one is located northward as *R* ratio increases.

4.3. Variation in the Position of the Triple Junction

Figure 12 summarizes the position of the triple junction as a function of *R*, as seen in our analog models: as this value increases, the triple junction is located more southwards in both single and two-stage models, which reflects the dominance of E-W trending faults (and a subordinate development of N-S faults propagating from the southern rift branch) as *R* increases. However, this apparent migration is less marked in the case of two-stage models (Figure 12b); despite the dominance of MP1 movement in the first stage, and the inheritance of E-W trending fault in the second stage, the high-angle fault interaction defining the triple junction results in it being located in a more northern position in two-stage models (e.g., cf., also the numerical models N-OR-5 and N-OR-6). This is likely associated with a weakening of the model crust which is already stretched during the first stage, inducing the abandonment of the southernmost E-W trending faults and allowing a more effective northward propagation of the subordinated N-S trending faults from the southern rift branch during the second stage (cf., as example single-stage model A-OR-5 and two-stage model A-OR-6 in Figures 13a and 13b), therefore causing a more northern triple junction.

Notably, considering the "kinematic triple junction" position as computed from McKenzie and Morgan (1969) and Gerya and Burov (2018) (Figure 12c), an opposite trend can be observed, with the junction locating progressively northward, as *R* ratio increases. This implies that the "structural triple junction," the "depositional triple junction" and the computed "kinematic triple junction" only coincide in the case of single-stage and totally symmetric junctions (i.e., $R = 1$).

4.4. Structural Triple Junction Migration With Time

Finally, analysis of model results highlights a general migration of the zone of fault interaction with time and progressive deformation, which is particularly evident for models with $R = 4$. For instance, when comparing

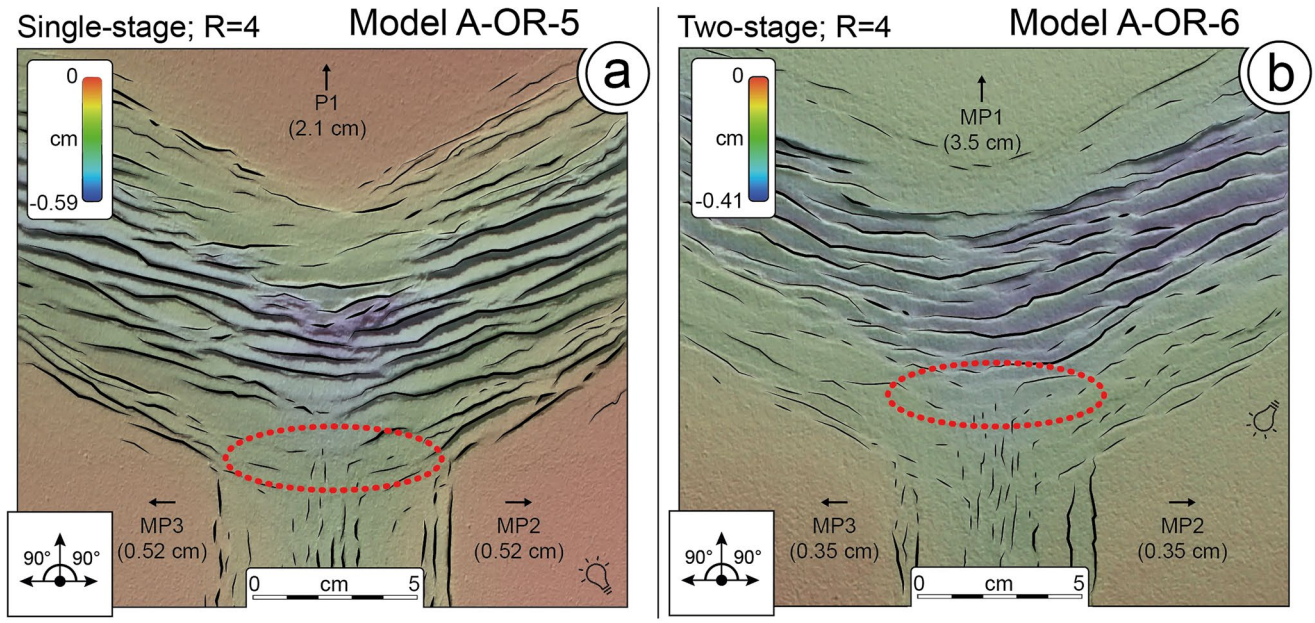

Figure 13. Comparison between single-stage and two-stage models of OR Series, with $R = 4$. (a) Model A-OR-5, run as a single-stage model. (b) Model A-OR-6, which experienced two extensional stages. The effect of a first extensional stage in model A-OR-6 (b) allows a more effective northward N-S trending fault propagation than in model with OR-5 with a single-stage. This effect is likely associated with a more strained LC in the two-stage model (b). The dashed red ellipse marks the triple junction location, defined as the place where high-angle fault interaction occurs.

time steps t_1 and t_2 for models A-SY-6 and A-OR-6 (both with $R = 4$) the location of the active triple junction (highlighted by a red dashed ellipse) clearly defines a northward migration trend (compare time t_1 and t_2 in Figures 14a–14d, respectively). This trend is shown also in our numerical models: in the asymmetric end-member N-OR-6, high-angle fault interaction progressively migrates northward with time (Figures 10e and 10f). These observations in the models agree with the hypothesis that different rates of extension across the rift segments of a RRR triple junction cause its migration through time (McKenzie & Morgan, 1969; Tesfaye et al., 2003). In contrast, similar velocities of the plates cause a stable triple junction location, as confirmed by our model SY-1 (Figures 3a–3c) with $R = 1$, (i.e., equal velocities for all plates).

4.5. Implications for Structural Evolution of the Afar Triple Junction

The Afar triple junction (Figures 15a and 15b) is the only Rift-Rift-Rift triple junction directly observable subaerially (Varet, 2018), and also a zone of incipient continental breakup. For this reason, it has been widely studied both at the local and regional scale (e.g., Almalki & Betts, 2021; Beyene & Abdelsalam, 2005; Burke & Dewey, 1973; DeMets & Merkouriev, 2021; Khalil et al., 2020, 2021; Koptev et al., 2018; Tesfaye et al., 2003; Varet, 2018; Wolfenden et al., 2004). Research has focused the debate on the influence of a mantle plume on the initiation of rifting (e.g., Burke & Dewey, 1973; Koptev et al., 2018) and the directions of propagation of the Red Sea, the Gulf of Aden and the Main Ethiopian Rift (MER) branches, but the primary controls on geometry and interaction of faults, along with the structural evolution through time remain poorly understood. Despite it is out of the aims of this work to settle the mantle-plume controversy (for an in-depth analysis the readers can further refer e.g., to Beyene and Abdelsalam [2005] and Varet [2018]), our comparison with the geometry of the Afar triple junction sheds light on some large-scale characteristics of its structural pattern and evolution with time.

Out of the two experimental Series, the most similar conditions to the current setting of the Afar case study are represented by the OR-Series, where an orthogonal extension was set between the moving plates MP2 and MP3, which represent the Somalian and Nubian plates, respectively (plate MP1 therefore simulates the Arabian Plate). At the Afar triple junction, faults exhibit high-angle interaction with the structures of the Main Ethiopian Rift, crosscutting the NW-SE and E-W trending faults (Figure 15b). This intersection results in a T-shaped fault pattern which is well reproduced in our analog (Figure 15c) and numerical models (Figure 15d) with high R ratio (e.g., $R = 4$). Such high R value simulates a scenario in which the northern plate (MP1) moves four times faster than

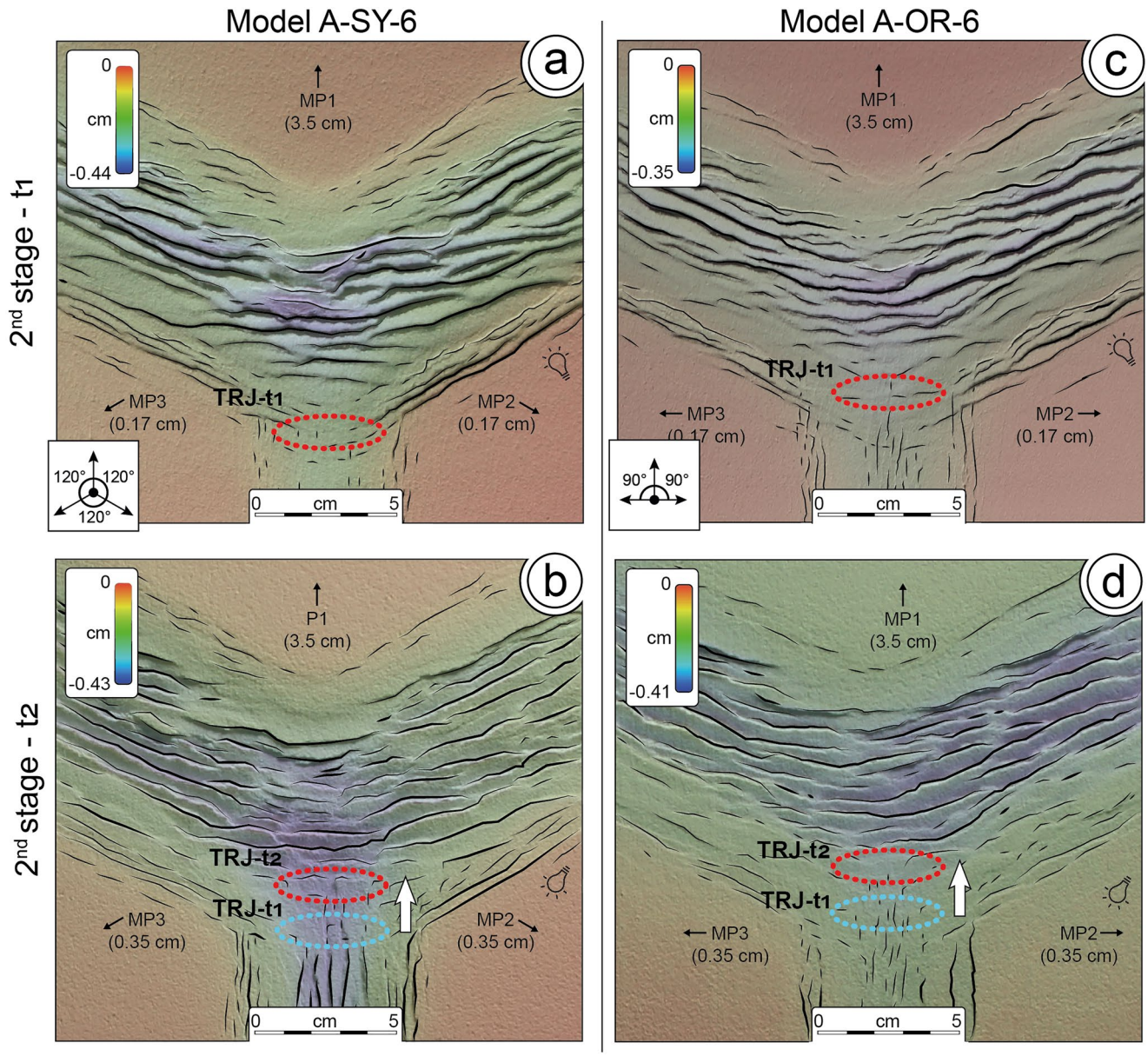

Figure 14. Comparison between A-SY-6 (a and c) and A-OR-6 models (c and d), with $R = 4$. The figure shows the two time steps occurring in the second stage of deformation for both models, highlighting the northward triple junction migration (thick white arrows) as model deformation proceeds. The red dashed ellipse marks the location of the active triple junction at time step t_1 (TRJ-t_1) and t_2 (TRJ-t_2), while the bluish dashed ellipse marks the relict location (TRJ-t_1) at time step t_2.

the other two moving plates, similarly to what occurs currently in Afar: the Arabian plate moves northwestward at ≈20 mm/yr relative to Nubia and Somalia (McClusky et al., 2010), while the Nubian and Somalian plates move apart at ≈5 mm/yr (Saria et al., 2014; Stamps et al., 2021).

While both single-stage and two-stage models with high R values exhibit the T-shaped fault pattern, this is more evident in the latter. In these models, the fault pattern associated with the southern and younger rift branch more efficiently propagate toward the triple junction, likely as a consequence of a more strained (and weakened) lower crust. This scenario replicates well the propagation of the axial faults in the MER northeastward toward the triple junction, intersecting at high angle with the NW-SE and E-W faults associated with Red Sea and Gulf of Aden rifting (Figure 15b). This similarity more strongly supports a two-stage history of interaction among the Arabian, Nubian and Somalian plates, and is a model result supported by plate kinematic modeling of real plate motions. Literature suggests that there was initial northward motion of Arabia with respect to Nubia/Somalia (at around 26–34 Ma),

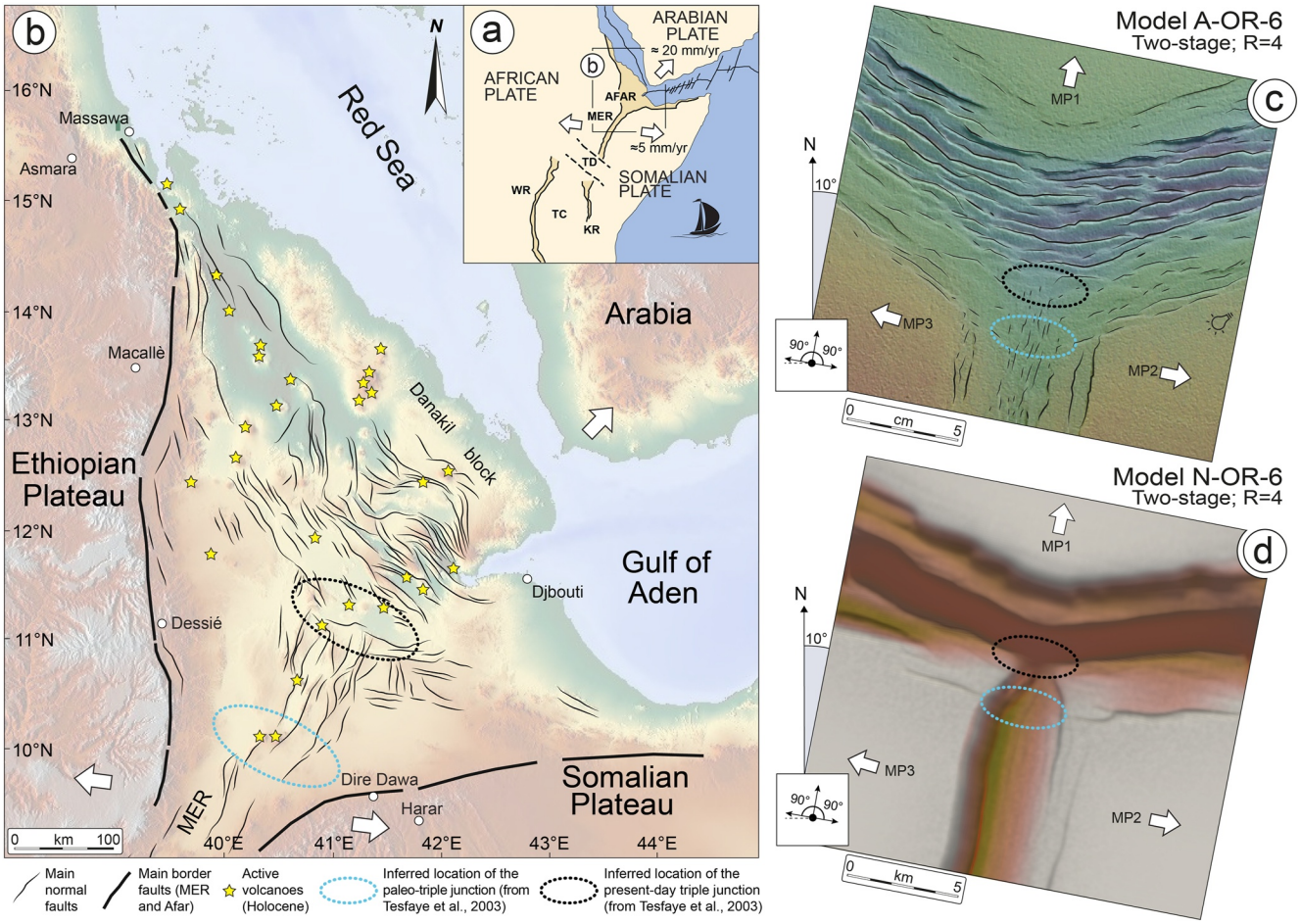

Figure 15. Comparison between analog and numerical models and the Afar triple junction. (a) The Afar triple junction and the East African Rift Systems. MER, Main Ethiopian Rift; TD, Turkana Depression; WR, Western Rift System; TC, Tanzania Craton; KR, Kenia Rift. Velocity vectors for the Arabian and Somalian plates are from McClusky et al. (2010), Saria et al. (2014), and Stamps et al. (2021). (b) Schematic structural setting of the Afar triple junction, showing similarities both with two-stage (c) analog and (d) numerical models with high R ration ($R = 4$). Map in (b) is modified from Sani et al., 2017. Base topography is from (data from the Shuttle Radar Topography Mission, SRTM; resolution 90 m). Structures are redrawn from Keir et al. (2013) after Manighetti et al. (2001). Models in (b) and (c) were rotated 10° clockwise to better fit with the natural case study.

followed by Nubia-Somalia divergence starting at around 16 Ma or later (DeMets & Merkouriev, 2021; Wolfenden et al., 2004) and suggesting that differential extension rates between the plates are key to explain the fault pattern at this Rift-Rift-Rift triple junction. Single and two-stage models with low R ratio show a symmetric Y-shaped fault pattern (cf., Figure 8) that is not compatible with the observed natural fault arrangement at the Afar junction.

Additionally, our models suggest that the area of maximum subsidence does not (always) correspond to the triple junction location (see Appendix A): this occurs in models with $R = 1$ but not in models with higher R values (e.g., $R = 4$). This mismatch is observed in Afar, where the area of maximum subsidence is currently located ~50–100 km NE of the triple junction. Geological studies including structural (Tesfaye et al., 2003; Wolfenden et al., 2004) and stratigraphic analysis (e.g., Alemseged et al., 2020; Campisano & Feibel, 2008; Kalb, 1995; Wynn et al., 2008) documented the northeastward migration of both the major depocenter in Afar, as well as the structural triple junction toward its present location (black and bluish dashed ellipses in Figure 15b), a feature directly related with different extensional in the three rift branches (McKenzie & Morgan, 1969). This triple junction migration with time is perfectly reproduced in our models: the close similarity between our models A-OR-6 and N-OR-6 with the current fault and depocenter geometry in Afar, coupled with available constraints on the past evolution of Afar, suggests that the high R ratio (i.e., marked differential velocity between rift branches) is fundamentally important in controlling the evolution of the triple junction architecture in Afar. In addition, our models suggest that the progressive northeastward migration of the main depocenter precedes migration of the triple junction.

The hypothesis of a two-stage extension history that is best-fit by our models, is also in agreement with previous analog models shown by Khalil et al. (2021) which suggest that triple junctions are unlikely to have been originated by a single-stage tectonic history. Furthermore, Khalil et al. (2020) suggested that triple junction dynamics in the Afar region likely did not cause the formation of the MER, this latter being related to a later and independent rifting event. This sequence is broadly supported by the majority of geological studies which suggest initiation of the Red Sea- Gulf of Aden rifting since 34 Ma, and the MER initiating at 10–20 Ma (e.g., Corti et al., 2022; Girdler, 1984; Watchorn et al., 1998; Wolfenden et al., 2004; Pik et al., 2013, and reference therein). Therefore, both our analog and numerical models, in agreement with other Authors (e.g., Almalki & Betts, 2021; Khalil et al., 2020, 2021), indicate that a simple single-stage, symmetric dynamic does not explain the structural pattern nowadays observed at the Afar triple junction, and its migration through time.

5. Concluding Remarks

We performed two experimental series of analog models, coupled with numerical models investigating Rift-Rift-Rift triple junction dynamics. We hereby define the structural triple junction as the area where faults related to the different motion of the three moving plates interact. Analog models simulated single and two tectonic stages, testing the effect of different velocity ratio (R) between plates and the direction of extension in one of the three rift branches (the southern one). Numerical models reproduced specific conditions applied to end-member (symmetric and asymmetric) analog models. The two approaches produced comparable results, suggesting that:

1. There are two distinct end-member geometries (symmetric, Y-shaped and asymmetric, T-shaped) as a function of the differential velocities applied to the moving plates. Hybrid structural patterns can occur for intermediate velocity conditions.
2. The number of tectonic stages can influence this geometry, with the asymmetric structural pattern being more evident in two-stage models.
3. Triple junction location strongly depends on the differential velocity between tectonic plates. High differential velocities between the reference and the other two tectonic plates (i.e., high R ratio) cause a structural triple junction located in a southern position. The triple junction locates in progressively northern position as the R ratio decreases, implying symmetric velocities condition.
4. Triple junction locations migrate through time in analog and numerical models with R larger than 1 ratio, moving northward as deformation proceeds. This is particularly evident in two-stage models, with a marked northward migration under orthogonal conditions of extension occurring in the southern rift branch.

Our results indicate that the structural pattern occurring at Rift-Rift-Rift triple junction is primarily dependent on the velocity conditions occurring at the three moving plates, with subordinated effects of the number of extensional stages and the direction of extension. When comparing these outcomes with the Afar case study, our models indicate that a two-stage tectonic history under differential extension conditions best reproduces observed natural fault patterns, such as the T-shaped fault interaction nowadays observable at the triple junction location. Our models therefore support the hypothesis of the northeastward triple junction migration through time.

Appendix A: Area of Maximum Subsidence

The moving plate MP1 can be taken as the reference plate as it is the only one among the three to keep constant its velocity and amount of displacement throughout models. It moves at 1 cm/hr for all models and covers the same total distance: 2.1 and 3.5 cm for single-stage and two-stage models, respectively. Therefore, its tip can be defined and used as a reference point (yellow star in Figures A1 and A2) for quantification of other parameters in the two experimental Series. We can identify the most depressed area located at the intersection between the three rift branches. The maximum subsidence is measured as relative depth in the triangular area obtained by linking the plate tips, and its distance from the MP1 tip can be measured and visualized on topographic profiles. Figure A1 shows the maximum subsidence position for single-stage models of SY (Figures A1a–A1c) and OR Series (Figures A1e–A1g). While model A-SY-1 (Figure A1a) shows a symmetric area of maximum subsidence, this becomes progressively asymmetric as the R value increases in models A-SY-3 and A-SY-5 (Figures A1b and A1c). Most interestingly, it migrates toward the reference point, as testified by the position of the depocenter (Figures A1a–A1d). Similarly, in OR models, the area of maximum subsidence migrates northward decreasing its distance from the reference point (Figures A1e–A1g and Figure 8h). Notably, in OR models, the shape of the

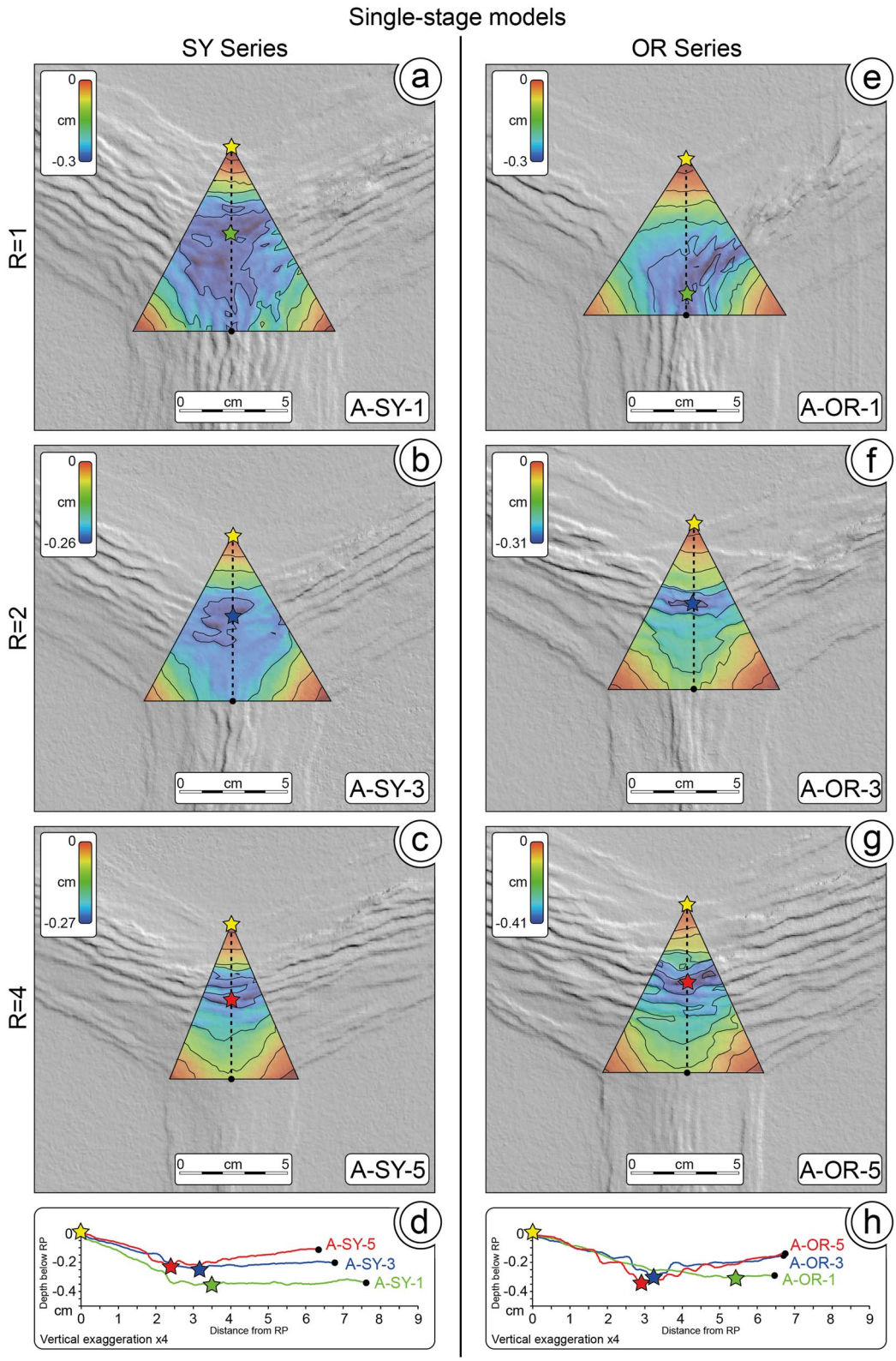

Figure A1. Area of maximum subsidence for single-stage models of SY Series (a–c) and OR Series (e–g). It is calculated in triangle defined by the tips of the three moving plates, so that the maximum depth values are rescaled for the triple junction area. The maximum subsidence progressively migrates northward as R value increases, as highlighted on topographic profiles (green, red and blue stars) in (d and h). Depth contours are shown every 0.5 mm. In the profiles, topography is normalized to a reference point (RP, yellow star; i.e., the topographic zero corresponds to the reference point corresponding to the tip of MP1 and all other values are rescaled accordingly as negative values).

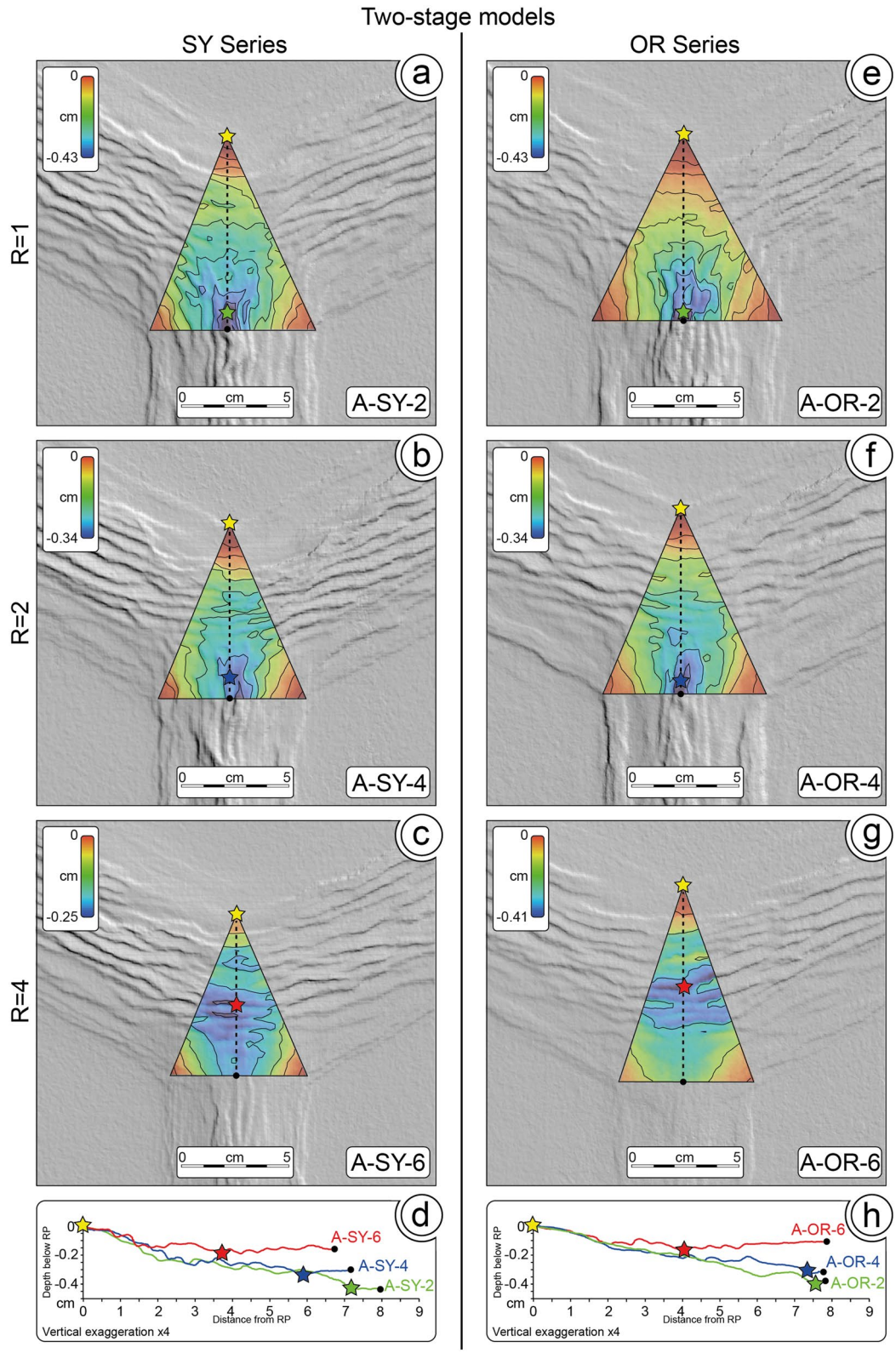

Figure A2. Area of maximum subsidence for two-stage models of SY Series (a–d) and OR Series (e–h), illustrated as in Figure A1.

area of maximum subsidence is less symmetric, a feature particularly evident in models A-OR-3 (Figure A1f) and A-OR-5 (Figure A1g), where it corresponds to E-W trending grabens associated with the dominant N-S trending MP1 movement, as the *R* value increases. This observation can be similarly made for two-stage models (Figure A2), and a northward migration of the area of maximum subsidence can be traced out.

This analysis indicates the maximum subsidence experiences a northward migration with increasing *R* ratio values throughout models and experimental series. This reflects the sole effect of a progressively more strained crust as the northward velocity component of MP1 increases with respect to the other two MPs. Nonetheless, despite showing this northward shift, its position remains located in a relatively southern area with respect to single-stage models (compare the maximum subsidence positions on profiles in Figures A2d and A2h). This may reflect the interaction with the N-S trending fault system, which propagates more northward in two-stage models. Moreover, the area of maximum subsidence results centered at the junction of the three rift branches only in the case of Y-shaped models (e.g., the end-member model A-SY-1) even during model evolution (e.g., cf., DEMs at time t_1, t_2, and t_3 in Figures 2a–2c), because of the symmetric direction of extension. Nonetheless, the triple junction and the area of maximum subsidence in most of cases do not coincide. This discrepancy is probably due to the strong control exerted by the *R* ratio on the area of maximum subsidence migration, while triple junction position reflects the coupled effect of the three investigated parameters.

Data Availability Statement

All the data supporting this research are available in the text, in Appendices, and in the in-text citation (Maestrelli et al., 2022), describing the data set supporting this manuscript, free to download from the GFZ data service repository at the link https://doi.org/10.5880/fidgeo.2022.027 under Creative Commons Attribution 4.0 International License.

Acknowledgments
We are grateful to the journal Reviewers Hany Mohamed Khalil and Taras Gerya, and to the Associate Editor Ernst Willingshofer for their precious comments, that greatly improved our work. We kindly acknowledge the Sibelco Italia S.p.A. in the person of Francesco Ferrari and his colleagues for kindly providing us part of the material used to run these experiments. This work was supported by Ministero dell'Università e della Ricerca (MiUR) through PRIN Grant 2017P9AT72 and by the (HLRN, https://www.hlrn.de/). Open Access Funding provided by Consiglio Nazionale delle Ricerche within the CRUI–CARE Agreement.

References

Alemseged, Z., Wynn, J. G., Geraads, D., Reed, D., Andrew Barr, W., Bobe, R., et al. (2020). Fossils from Mille-Logya, Afar, Ethiopia, elucidate the link between Pliocene environmental changes and Homo origins. *Nature Communications*, *11*(1), 1–12. https://doi.org/10.1038/s41467-020-16060-8

Almalki, K. A., & Betts, P. G. (2021). Gulf of Aden spreading does not conform to triple-junction formation. *Geology*, *49*(6), 672–67. https://doi.org/10.1130/G48529.1

Beyene, A., & Abdelsalam, M. G. (2005). Tectonics of the Afar depression: A review and synthesis. *Journal of African Earth Sciences*, *41*(1–2), 41–59. https://doi.org/10.1016/j.jafrearsci.2005.03.003

Burke, K., & Dewey, J. F. (1973). Plume-generated triple junctions: Key indicators in applying plate tectonics to old rocks. *The Journal of Geology*, *81*(4), 406–433. https://doi.org/10.1086/627882

Campisano, C. J., & Feibel, C. S. (2008). Depositional environments and stratigraphic summary of the Pliocene Hadar formation at Hadar, Afar depression, Ethiopia. *The geology of early humans in the Horn of Africa*, *446*, 179–201. https://doi.org/10.1130/2008.2446(08)

Corti, G., Cioni, R., Franceschini, Z., Sani, F., Scaillet, S., Molin, P., et al. (2019). Aborted propagation of the Ethiopian rift caused by linkage with the Kenyan rift. *Nature Communications*, *10*(1), 1309. https://doi.org/10.1038/s41467-019-09335-2

Corti, G., Maestrelli, D., & Sani, F. (2022). Large-to local-scale control of pre-existing structures on continental rifting: Examples from the Main Ethiopian Rift, East Africa. *Frontiers in Earth Science*, *10*, 46. https://doi.org/10.3389/feart.2022.808503

Del Ventisette, C., Bonini, M., Agostini, A., Corti, G., Maestrelli, D., & Montanari, D. (2019). Using different grain-size granular mixtures (quartz and K-feldspar sand) in analog extensional models. *Journal of Structural Geology*, *129*, 103888. https://doi.org/10.1016/j.jsg.2019.103888

DeMets, C., & Merkouriev, S. (2021). Detailed reconstructions of India–Somalia Plate motion, 60 Ma to present: Implications for Somalia Plate absolute motion and India–Eurasia Plate motion. *Geophysical Journal International*, *227*(3), 1730–1767. https://doi.org/10.1093/gji/ggab295

Donnadieu, F., Kelfoun, K., de Vries, B. V. W., Cecchi, E., & Merle, O. (2003). Digital photogrammetry as a tool in analog modeling: Applications to volcano instability. *Journal of Volcanology and Geothermal Research*, *123*(1–2), 161–180. https://doi.org/10.1016/S0377-0273(03)00034-9

Dordevic, M., & Georgen, J. (2016). Dynamics of plume–triple junction interaction: Results from a series of three-dimensional numerical models and implications for the formation of oceanic plateaus. *Journal of Geophysical Research: Solid Earth*, *121*(3), 1316–1342. https://doi.org/10.1002/2014JB011869

Georgen, J. E., & Lin, J. (2002). Three-dimensional passive flow and temperature structure beneath oceanic ridge–ridge–ridge triple junctions. *Earth and Planetary Science Letters*, *204*(1–2), 115–132. https://doi.org/10.1016/S0012-821X(02)00953-6

Gerya, T., & Burov, E. (2018). Nucleation and evolution of ridge-ridge-ridge triple junctions: Thermomechanical model and geometrical theory. *Tectonophysics*, *746*, 83–105. https://doi.org/10.1016/j.tecto.2017.10.020

Girdler, R. W. (1984). The evolution of the Gulf of Aden and Red Sea in space and time. *Deep Sea Research Part A. Oceanographic Research Papers*, *31*(6–8), 747–762. https://doi.org/10.1016/0198-0149(84)90039-6

Glerum, A., Brune, S., Stamps, D. S., & Strecker, M. R. (2020). Victoria continental microplate dynamics controlled by the lithospheric strength distribution of the East African Rift. *Nature Communications*, *11*(1), 2881. https://doi.org/10.1038/s41467-020-16176-x

Glerum, A., Thieulot, C., Fraters, M., Blom, C., & Spakman, W. (2018). Nonlinear viscoplasticity in ASPECT: Benchmarking and applications to subduction. *Solid Earth*, *9*(2), 267–294. https://doi.org/10.5194/se-9-267-2018

Gouiza, M., & Naliboff, J. (2021). Rheological inheritance controls the formation of segmented rifted margins in cratonic lithosphere. *Nature Communications*, *12*(1), 4653. https://doi.org/10.1038/s41467-021-24945-5

Hayward, N. J., & Ebinger, C. J. (1996). Variations in the along-axis segmentation of the Afar Rift system. *Tectonics*, *15*(2), 244–257. https://doi.org/10.1029/95TC02292

Heckenbach, E. L., Brune, S., Glerum, A. C., & Bott, J. (2021). Is there a speed limit for the thermal steady-state assumption in continental Rifts? *Geochemistry, Geophysics, Geosystems*, *22*(3), e2020GC009577. https://doi.org/10.1029/2020GC009577

Heister, T., Dannberg, J., Gassmöller, R., & Bangerth, W. (2017). High accuracy mantle convection simulation through modern numerical methods – II: Realistic models and problems. *Geophysical Journal International*, *210*(2), 833–851. https://doi.org/10.1093/gji/ggx195

Hubbert, M. K. (1937). Theory of scale models as applied to the study of geologic structures. *Bulletin of the Geological Society of America*, *48*(10), 1459–1520. https://doi.org/10.1130/GSAB-48-1459

Jestin, F., & Huchon, P. (1992). Kinematics and deformation of the Red Sea-Gulf of Aden-Ethiopian Rift triple junction since the Oligocene. *International Geology Review*, *34*(10), 961–975. https://doi.org/10.1080/00206819209465646

Kalb, J. (1995). Fossil elephantoids, Awash paleolake basins, and the Afar triple junction, Ethiopia. *Palaeogeography, Palaeoclimatology, Palaeoecology*, *114*(2–4), 357–368. https://doi.org/10.1016/0031-0182(94)00088-P

Karaoğlu, Ö., Browning, J., Bazargan, M., & Gudmundsson, A. (2016). Numerical modeling of triple-junction tectonics at Karlıova, Eastern Turkey, with implications for regional magma transport. *Earth and Planetary Science Letters*, *452*, 157–170. https://doi.org/10.1016/j.epsl.2016.07.037

Keir, D., Bastow, I. D., Pagli, C., & Chambers, E. L. (2013). The development of extension and magmatism in the Red Sea rift of Afar. *Tectonophysics*, *607*, 98–114. https://doi.org/10.1016/j.tecto.2012.10.015

Khalil, H. M., Capitanio, F. A., Betts, P. G., & Cruden, A. R. (2020). 3-D analog modeling constraints on rifting in the Afar region. *Tectonics*, *39*(10), e2020TC006339. https://doi.org/10.1029/2020TC006339

Khalil, H. M., Capitanio, F. A., & Cruden, A. R. (2021). The evolution of triple junctions: From failure to success. Eartharxiv preprint. https://doi.org/10.31223/X5FK7Z

Kleinrock, M. C., & Morgan, J. P. (1988). Triple junction reorganization. *Journal of Geophysical Research*, *93*(B4), 2981–2996. https://doi.org/10.1029/JB093iB04p02981

Koptev, A., Gerya, T., Calais, E., Leroy, S., & Burov, E. (2018). Afar triple junction triggered by plume-assisted bi-directional continental break-up. *Scientific Reports*, *8*(1), 1–7. https://doi.org/10.1038/s41598-018-33117-3

Kronbichler, M., Heister, T., & Bangerth, W. (2012). High accuracy mantle convection simulation through modern numerical methods. *Geophysical Journal International*, *191*(1), 12–29. https://doi.org/10.1111/j.1365-246X.2012.05609.x

Leroy, S., Razin, P., Autin, J., Bache, F., D'Acremont, E., Watremez, L., et al. (2012). From rifting to oceanic spreading in the Gulf of Aden: A synthesis. *Arabian Journal of Geosciences*, *5*(5), 859–901. https://doi.org/10.1007/s12517-011-0475-4

Maestrelli, D., Bonini, M., Corti, G., Del Ventisette, C., Moratti, G., & Montanari, D. (2021a). A database of laboratory analog models of caldera collapse testing the role of inherited structures. *Frontiers in Earth Science*, *9*, 27. https://doi.org/10.3389/feart.2021.618258

Maestrelli, D., Bonini, M., Corti, G., Del Ventisette, C., Moratti, G., & Montanari, D. (2021b). Exploring fault propagation and the role of inherited structures during caldera collapse through laboratory experiments. *Journal of Volcanology and Geothermal Research*, *414*, 107232. https://doi.org/10.1016/j.jvolgeores.2021.107232

Maestrelli, D., Montanari, D., Corti, G., Del Ventisette, C., Moratti, G., & Bonini, M. (2020). Exploring the interactions between rift propagation and inherited crustal fabrics through experimental modeling. *Tectonics*, *39*(12), e2020TC006211. https://doi.org/10.1029/2020TC006211

Maestrelli, D., Risaliti, G., Brune, S., Corti, G., Keir, D., & Sani, F. (2022). A database of R-R-R triple junction analogue and numerical models. *GFZ Data Services*. https://doi.org/10.5880/fidgeo.2022.027

Manighetti, I., Tapponier, P., Courtillot, V., Gallet, Y., Jacques, E., & Gillot, P. Y. (2001). Strain transfer between disconnected, propagating rifts in Afar. *Journal of Geophysical Research*, *106*(B7), 13613–13665. https://doi.org/10.1029/2000JB900454

Manighetti, I., Tapponnier, P., Courtillot, V., Gruszow, S., & Gillot, P. Y. (1997). Propagation of rifting along the Arabia-Somalia plate boundary: The gulfs of Aden and Tadjoura. *Journal of Geophysical Research*, *102*(B2), 2681–2710. https://doi.org/10.1029/96JB01185

McClusky, S., Reilinger, R., Ogubazghi, G., Amleson, A., Healeb, B., Vernant, P., et al. (2010). Kinematics of the southern Red Sea–Afar Triple Junction and implications for plate dynamics. *Geophysical Research Letters*, *37*(5). https://doi.org/10.1029/2009GL041127

McKenzie, D. P., & Morgan, W. J. (1969). Evolution of triple junctions. *Nature*, *224*(5215), 125–133. https://doi.org/10.1038/224125a0

Montanari, D., Agostini, A., Bonini, M., Corti, G., & Ventisette, C. (2017). The use of empirical methods for testing granular materials in analog modeling. *Materials*, *10*(6), 635. https://doi.org/10.3390/ma10060635

Naliboff, J., Glerum, A., Brune, S., Péron-Pinvidic, G., & Wrona, T. (2020). Development of 3-D rift heterogeneity through fault network evolution. *Geophysical Research Letters*, *47*(13), e2019GL086611. https://doi.org/10.1029/2019GL086611

Neuharth, D., Brune, S., Wrona, T., Glerum, A., Braun, J., & Yuan, X. (2022). Evolution of rift systems and their fault networks in response to surface processes. *Tectonics*, *41*(3), e2021TC007166. https://doi.org/10.1029/2021TC007166

Oliveira, M. E., Gomes, A. S., Duarte, J. C., França, G. S., Rosas, F. M., Fuck, R. A., & Silva, F. A. (2021). Evolution of parallel, oblique and triple-junction rifts: Insights from analog modeling. *Journal of South American Earth Sciences*, *110*, 103394. https://doi.org/10.1016/j.jsames.2021.103394

Patriat, P., & Courtillot, V. (1984). On the stability of triple junctions and its relation to episodicity in spreading. *Tectonics*, *3*(3), 317–332. https://doi.org/10.1029/TC003i003p00317

Pik, R., Bellahsen, N., Leroy, S., Denèle, Y., Razin, P., Ahmed, A., & Khanbari, K. (2013). Structural control of basement denudation during rifting revealed by low-temperature (U-Th-Sm)/He thermochronology of the Socotra Island basement—Southern Gulf of Aden margin. *Tectonophysics*, *607*, 17–31. https://doi.org/10.1016/j.tecto.2013.07.038

Ramberg, H. (1981). *Gravity, deformation, and the Earth's crust: In theory, experiments, and geological application*. Academic Press.

Richter, M. J. E. A., Brune, S., Riedl, S., Glerum, A., Neuharth, D., & Strecker, M. R. (2021). Controls on asymmetric rift dynamics: Numerical modeling of strain localization and fault evolution in the Kenya Rift. *Tectonics*, *40*(5), e2020TC006553. https://doi.org/10.1029/2020TC006553

Rose, I., Buffett, B., & Heister, T. (2017). Stability and accuracy of free surface time integration in viscous flows. *Physics of the Earth and Planetary Interiors*, *262*, 90–100. https://doi.org/10.1016/j.pepi.2016.11.007

Sani, F., Ghinassi, M., Papini, M., Oms, O., & Finotello, A. (2017). Evolution of the northern tip of Afar triangle: Inferences from the Quaternary succession of the Dandiero—Massawa area (Eritrea). *Tectonophysics*, *717*, 339–357. https://doi.org/10.1016/j.tecto.2017.08.026

Saria, E., Calais, E., Stamps, D. S., Delvaux, D., & Hartnady, C. J. H. (2014). Present-day kinematics of the East African Rift. *Journal of Geophysical Research: Solid Earth*, *119*(4), 3584–3600. https://doi.org/10.1002/2013JB010901

Schellart, W. P., & Strak, V. (2016). A review of analogue modelling of geodynamic processes: Approaches, scaling, materials and quantification, with an application to subduction experiments. *Journal of Geodynamics*, *100*, 7–32. https://doi.org/10.1016/j.jog.2016.03.009

Schonberger, J. L., & Frahm, J. M. (2016). Structure-from-motion revisited. In *Proceedings of the IEEE Conference on Computer Vision and Pattern Recognition* (pp. 4104–4113).

Souriot, T., & Brun, J. P. (1992). Faulting and block rotation in the Afar triangle, East Africa: The Danakil "crank-arm" model. *Geology*, *20*(10), 911–914. https://doi.org/10.1016/j.jsames.2021.103394

Stamps, D. S., Kreemer, C., Fernandes, R., Rajaonarison, T. A., & Rambolamanana, G. (2021). Redefining east African rift system kinematics. *Geology*, *49*(2), 150–155. https://doi.org/10.1130/G47985.1

Stein, C. A., Stein, S., Gallahue, M. M., & Elling, R. P. (2022). Revisiting hotspots and continental breakup—Updating the classical three-arm model. https://doi.org/10.1130/2021.2553(05)

Tesfaye, S., Harding, D. J., & Kusky, T. M. (2003). Early continental breakup boundary and migration of the Afar triple junction, Ethiopia. *Geological Society of America Bulletin*, *115*(9), 1053–1067. https://doi.org/10.1130/B25149.1

Varet, J. (2018). *Geology of Afar (East Africa)* (p. 336). Springer. https://doi.org/10.1007/978-3-319-60865-5

Wang, L., Maestrelli, D., Corti, G., Zou, Y., & Shen, C. (2021). Normal fault reactivation during multiphase extension: Analog models and application to the Turkana depression, East Africa. *Tectonophysics*, *811*, 228870. https://doi.org/10.1016/j.tecto.2021.228870

Watchorn, F., Nichols, G. J., & Bosence, D. W. J. (1998). Rift-related sedimentation and stratigraphy, southern Yemen (Gulf of Aden). In *Sedimentation and Tectonics in Rift Basins: Red Sea, Gulf of Aden* (pp. 165–189). Springer. https://doi.org/10.1046/j.1365-3091.2001.0394b.x

Weijermars, R. (1997). *Principles of rock mechanics*. Alboran Science Publishing.

Weijermars, R., & Schmeling, H. (1986). Scaling of Newtonian and non-Newtonian fluid dynamics without inertia for quantitative modeling of rock flow due to gravity (including the concept of rheological similarity). *Physics of the Earth and Planetary Interiors*, *43*(4), 316–330. https://doi.org/10.1016/0031-9201(86)90021-x

Wolfenden, E., Ebinger, C., Yirgu, G., Deino, A., & Ayalew, D. (2004). Evolution of the northern Main Ethiopian Rift: Birth of a triple junction. *Earth and Planetary Science Letters*, *224*(1–2), 213–228. https://doi.org/10.1016/j.epsl.2004.04.022

Wynn, J. G., Roman, D. C., Alemseged, Z., Reed, D., Geraads, D., & Munro, S. (2008). Stratigraphy, depositional environments, and basin structure of the Hadar and Busidima Formations at Dikika, Ethiopia. *Geological Society of America Special Paper*, *446*, 87–118. https://doi.org/10.1130/2008.2446(04)